Carl von Ossietzky Universität Oldenburg

DLR Deutsches Zentrum für Luft- und Raumfahrt
German Aerospace Center
Institute of Networked Energy Systems

Masterthesis

A Tunnel Recombination Junction for the Integration of a TiO_x-Photoanode on a Silicon Wafer for Solar Water Splitting

DLR Institute for Networked Energy Systems and

Carl von Ossietzky University Oldenburg

1st supervisor: Prof. Dr. Carsten Agert
2nd supervisor: Dr. Martin Vehse

Luisa Busch
Matr. nr.: 5559957
Physics (M. Sc.)
Oldenburg, May 22, 2023

Contents

1 Introduction **1**

2 Theoretical Background **3**
2.1 Energetic Properties of Semiconductors 3
2.1.1 The Band Gap 3
2.1.2 Charge Carrier Concentrations in Equilibrium 4
2.1.3 Photoabsorption - Charge Carriers in Non-equilibrium 8
2.1.4 Energy Forms of Electrons and Holes 9
2.1.5 Transport Mechanisms of Free Charge Carriers 10
2.1.6 The Conductivity of Semiconductors 11
2.2 Semiconductor Junctions 12
2.2.1 Standard p-n-Junction 12
2.2.2 Tunnel Recombination Junctions 14
2.2.3 Semiconductor Metal Junction 17
2.2.4 Semiconductor Electrolyte Interface 18
2.3 Photoelectrochemical Cells 19
2.3.1 Photoelectrochemical Water Splitting 19
2.3.2 Working Principle 20
2.3.3 Tandem PEC and its Limitations 21
2.4 Hybrid Photoelectrochemical- and Voltaic Cells 21
2.5 Semiconductor Materials 22
2.5.1 Silicon 23
2.5.2 TiO_x 23

3 Experimental Methods **25**
3.1 Sample Manufacturing 25
3.1.1 Plasma-enhanced Chemical Vapor Deposition 25
3.1.2 Physical Vapor Deposition - Reactive Sputtering 27
3.1.3 Electron Beam Physical Vapor Deposition 29
3.2 Sample Characterization 29
3.2.1 UV-Vis Optical Spectrometry 29
3.2.2 Dark Conductivity 30
3.2.3 Hall Effect Measurement 31
3.2.4 Raman Spectroscopy 32
3.2.5 Profilometer 34
3.2.6 Linear Sweep Voltammetry 35

4 Interlayer Material Selection **38**

4.1 Requirements for the Interlayer . . . 38
4.2 P-type TRJ Materials . . . 40
4.3 Chosen Material and Sample Setup . . . 41

5 Stack Preparation 44
5.1 Sample Stack . . . 44
5.2 Wafer Backside . . . 44
5.2.1 Raman Deconvolution . . . 45
5.2.2 Layer Thickness . . . 45
5.2.3 Tauc Optical Band Gap . . . 46
5.2.4 Dark Conductivity . . . 47

6 Proof-Of-Concept 49
6.1 Aim of the Experiment . . . 49
6.2 Experimental Setup . . . 49
6.3 Results and Discussion . . . 50
6.3.1 Raman Deconvolution . . . 50
6.3.2 Layer Thickness . . . 53
6.3.3 Tauc Optical Band Gap . . . 53
6.3.4 Dark Conductivity . . . 55
6.3.5 Electrochemical Characterization . . . 56

7 Comparison with a TiO2 Photoanode 61
7.1 Aim of the Experiment . . . 61
7.2 Experimental Setup . . . 61
7.3 Results and Discussion . . . 62
7.3.1 Raman Spectroscopy . . . 62
7.3.2 Layer Thickness . . . 62
7.3.3 Electrochemical Characterization . . . 63

8 Device Degradation 67
8.1 Aim of the Experiment . . . 67
8.2 Experimental Setup . . . 67
8.3 Results and Discussion . . . 67

9 Summary and Conclusion 70

References 71

List of Figures

1 Schematic representation of the energy bands for metal, semiconductor and insulator materials. 4
2 Illustration of the different relative positions of the Fermi level inside the band gap for intrinsic, n-type and p-type semiconductors 7
3 Different energy forms for electrons and holes in a semiconductor. 9
4 Schematic representation of electron energies in a semiconductor in equilibrium with both electrostatic and chemical potential gradients. 11
5 Schematic representation of the energy band diagram in a p-n-junction in equilibrium and in non-equilibrium with quasi fermi level splitting. . 13
6 Schematic representation of quantum tunneling. 15
7 Schematic sketch of a tunnel recombination junction energy band diagram. 16
8 Schematic representation of the energy band diagram of a Si/perovskite tandem solar cell with tunnel recombination junction. 17
9 Schematic representation of the energy band diagrams for ohmic and Schottky metal-semiconductor contacts. 18
10 Schematic representation of the working principle of a PEC. 20
11 Schematic representation of the working principle of an HPEV cell. . . . 22
12 Schematic representation of crystalline and amorphous silicon. 23
13 Schematic representation of the different polymorphs of TiO_2. 24
14 Schematic representation of a plasma-enhanced chemical vapor deposition process. 26
15 Schematic representation of an RF reactive magnetron sputtering process. 28
16 Schematic representation of the principle behind Hall effect measurement. 31
17 Principle of different molecule scattering forms inclusive Raman scattering. 33
18 Example plot for deconvolution of Raman spectrum for determination of silicon crystallinity. 34
19 Experimental setup for linear sweep voltammetry. 35
20 Example of a linear scan voltammetry result for an n-type $BiVO_4$ photoanode. 36
21 Experimental setup design for linear scan voltammetry. 37
22 Band diagram of the two semiconductors in direct contact without an interlayer, simulated with AFORS-HET. 39
23 Schematic representation of a TRJ by the location of the energy band edges of each layer in a perovskite CIGS tandem solar cell 40
24 Schematic representation of the TRJ between TiO_2 and an n-type Si layer realized by a n^{++}/p^{++} TRJ. 41

26 Layer stack as used in this work including approximate layer thicknesses and the corresponding deposition method 44
29 Absorption coefficient and tauc plot for an exemplary nc-Si(n) single layer on a glass substrate. 47
31 Schematic representation of the sample setup for the first experiment. . 49
32 Raman signal deconvolution of nc-Si(p) layers 51
34 Absorption coefficients and tauc plots for all three nc-Si(p) single layers on glass substrate of the experiment. 54
35 Arrhenius plots as the results of dark conductivity measurements for the nc-Si(p) single layers. 55
36 Linear sweep voltammogramms for all samples of the experiment. 57
37 Linear sweep voltammetry plots of the Proof-of-Concept experiment for all samples, plotted for all light measurements seperated according to the number of light measurement. 58
38 Schematic representation of the sample setup for the comparison with a TiO_2 Photoanode. 61
39 Raman signal of the photoanode layers. 62
40 Linear sweep voltammogramms for every sample. 64
41 Linear sweep voltammograms for the three samples in this experiment showing the first (a), second (b) and third (c) LSV measurements under irradiation. 65
42 Linear sweep voltammogramms of one PEC device for 10 consecutive light measurements. 68

List of Tables

1 Summary of different parameter definitions for the three semiconductor types intrinsic, n-type and p-type. 8
2 Properties of the materials Si wafer and TiOx photoanode used for the band diagram simulation in this work. 38
3 Parameters for the PECVD process during nc-Si(p) deposition 50
4 Crystallinity factors of the nc-Si(p) layers. 52
5 Measured thicknesses of the nc-Si(p) layers 53
6 Tauc optical band gaps resulting from the linear fit to the tauc plots. . . 54
7 Current densities at 0 V and 1.23 V vs RHE and the maximum current densities at 1.7 V vs Ag/AgCl. 59
8 Measured thicknesses of the TiO_x and TiO_2 layers 63

1 Introduction

The climate targets set in the Paris Agreement to limit global warming to at least 2 °C, better 1.5 °C, in comparison to pre-industrial levels [1] require carbon-neutrality until the middle of the current century [2]. To achieve this, an energy transition towards renewable energy sources is necessary and can not be done without energy storage concepts to buffer the intermittent generation of renewables [3]. The chemical storage of energy is a promising concept. Hydrogen thereby was found to be advantageous due to its low self-discharge and its applicability as a fuel (in fuel-cells or combustion engines), what makes it a versatile storage medium [3]. A very promising way of storing renewable energies in the form of hydrogen is by solar energy conversion via photoelectrochemical watersplitting with so called photoelectrochemical cells (PEC), which was first presented by Fujishima and Honda in 1972 [4]. The cell consisted of the semiconductor material Titaniumdioxide (TiO_2) for the voltage supply to drive the chemical reactions and an electrolyte for the supply of hydrogen ions.

TiO_2 is a widely used material for photoelectrochemical water splitting due to its high stability and its suitable optoelectronic properties [5, 6]. To increase the absorption of TiO_2 as a photoanode, Berends et al. [7] developed a sub-stoichiometric TiO_x photoanode with higher absorption. For efficient use of the solar energy, tandem cells with different band gap materials are used. A further increase in efficiency was reached in 2018 by Segev et al. [8]. They showed that the simultaneous production of electricity and hydrogen by a single device could represent a significant increase in energy return on energy investment in comparison to a standard PEC. For their so-called hybrid photoelectrochemical and -voltaic cell they integrated a TiO_2 layer on an interdigitated back contact (IBC) Si wafer. With the two contacts on the back and the contact on the front side of the cell, two circuits can be set up. One circuit enables solar water splitting, while the other takes the excess charge carriers to create a PV circuit. This means that the solar energy can be converted into hydrogen and electricity at the same time.

In perspective, the understrochiometric TiO_x photoanode developed by Berends et al. should be integrated onto an IBC wafer as an HPEV device. For an efficient charge extraction of the photo-induced charge carriers, the band alignment of the different layers inside the cell plays a major role (see chapter 2.2).

Therefore, this work aims to develop a concept for the integration of the photoanode developed by Berends et al. onto an IBC wafer. To make the system simpler and less complex, a conventional, untreated crystalline n-type silicon wafer was used instead of an IBC wafer, to create a tandem photoelectrochemical cell.

As a first step for the development of the tandem cell, the two existing semiconductor

materials are characterized to determine whether additional layers are required and, if so, to derive a promising layer concept. Since it turns out that an intermediate layer is necessary, a possible material for such an interlayer will be identified. Subsequently, a practical check will be carried out to determine whether the material is suitable for the laboratory conditions in order to improve the cell performance of the tandem PEC. Since the very first cells of this kind will be produced in the existing laboratory conditions, an important goal is to produce functioning tandem PECs and to ensure that the results can be attributed to successful integration.

Within this thesis, first the necessary theoretical basics for understanding about tandem PECs and the processes that take place inside the cells are presented. Then, the methods of sample preparation and characterization used in this thesis are explained. This is followed by the chapter dealing with the selection of material for the interlayer. Next, the results of the proof-of-concept experiment are presented and discussed. After that, a comparison is made between TiO_x and TiO_2 as photoanode in PEC. This is followed by a chapter that addresses the degradation observed during the LSV measurements. The work is rounded off by a summary and a conclusion.

2 Theoretical Background

The total current of a PEC and also a HPEV results from successful separation of photoinduced free charge carriers in the materials before they recombine. The efficiency of charge carrier generation and separation depends on many factors, such as band gaps, charge carrier concentrations, or band alignment of the individual layers within the cell. Therefore, in this chapter the processes of free charge carrier generation, separation and extraction in photoelectrochemical cells are explained. First, with the explanation of band gap, charge carrier concentration and the Fermi level in equilibrium, i.e. in the dark, the energetic properties of semiconductor materials are presented. In contrast to this, the semiconductor in non-equilibrium, i.e. under illumination, is considered next. In order to understand the processes within the semiconductor junctions, the energy forms of the charge carriers as well as the resulting transport mechanisms and conductivity are presented. In the next subsection, the different junctions within photoelectrochemical devices are explained with a focus on the p-n-junction and the tunnel recombination junction. The next chapter is devoted to photoelectrochemical water splitting using photoelectrochemical cells. Not only is the working principle explained, but also the need for tandem PECs and their limitations are outlined. At the end, an outlook on the concept of an HPEV is given.

2.1 Energetic Properties of Semiconductors

Semiconductor materials are particularly suitable as absorber materials for photovoltaic and photoelectrochemical cells. They are characterized by the fact that their conductivity lies between that of metals and insulators.

2.1.1 The Band Gap

The reason for the different conductivities lies in the respective arrangement of the energy bands of metals, semiconductors and insulators. Energy bands represent energetic regions with a continuous distribution of electron states, within which and between which electrons can move by the transfer of energy. In single atoms, the energy levels appear as discrete values. When a solid is formed out of several atoms, they split off into so many values that they form a continuum of energy bands. However, there are energy intervals in which no electronic states exist, the so-called energy band gaps E_g. Figure 1 shows the different occupation of energy bands for the three materials. If a band is completely filled with electrons, it cannot be electrically conductive as there are no empty states available to move to. The valence band is the filled energy band with the highest energy. The next higher band is empty or partly filled and can therefore be conductive - the so called conduction band. Only the lifting of electrons into the conduction band leads to the fact that now both bands are no longer completely filled

and thus an electrical conduction becomes possible. The greater the energetic amount required to lift an electron into the conduction band, the lower the corresponding conductivity of the material.

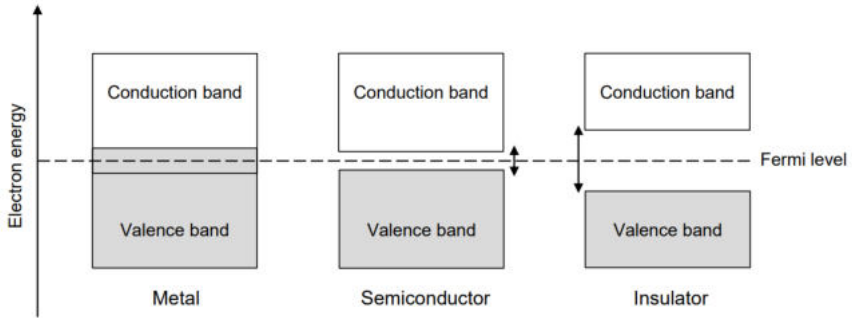

Figure 1: Schematic representation of the energy bands for metal, semiconductor and insulator materials. The grey coloring indicates a filling with electrons. For metals, valence and conduction bands overlap - the conduction band is already partially filled with electrons. For the semiconductor and insulator, a clear gap of forbidden energy states - the band gap - can be seen. For the semiconductor, this energy gap is clearly smaller. The Fermi level, a characteristic parameter for electron distribution, is shown. More details to the Fermi level are given in the next subsection. Own representation based on [9].

Metals already have a half-filled conduction band at absolute zero, so that conductivity is present. The reason behind this is the overlapping of valence and conduction band, so the absence of an energy band gap E_g. Semiconductors and insulators, on the other hand, have a band gap that electrons must first overcome by absorbing energy (e.g. from photons) in order to generate conductivity. For semiconductor materials, this required energy is about $0.5 - 3.0$ eV. Insulators usually have a band gap above 5 eV. [10, 11]

2.1.2 Charge Carrier Concentrations in Equilibrium

The distribution of electrons in semiconductors follows the Fermi-Dirac distribution, which describes the probability $f(E)$ that an energy level E is occupied by an electron as follows:

$$f(E) = \frac{1}{\exp\frac{E-E_\mathrm{F}}{kT} + 1}, \tag{1}$$

where k describes the Boltzmann constant being $k = 1.38 \times 10^{-23}\,\mathrm{J/K}$, T the temperature in K and E_F the Fermi energy. At absolute zero, i.e. at $T = 0\,\mathrm{K}$, the probability of finding an electron at an energy that is greater than the fermi level is zero, so $f(E > E_\mathrm{F}) = 0$, since no energy is supplied to the system and thus no electrons can

be lifted into the conduction band. All electrons are therefore below the Fermi energy, so $f(E < E_\mathrm{F}) = 1$. As soon as excitations into the conduction band can occur, i.e. as soon as $T > 0\,\mathrm{K}$, the Fermi energy describes the energy at which the distribution function is exactly $f(E = E_\mathrm{F}) = \frac{1}{2}$. For systems with $E_\mathrm{F} < E_\mathrm{C} - 3kT$ the Boltzmann approximation is valid with

$$f(E) = \frac{1}{\exp\frac{E-E_\mathrm{F}}{kT}} \ . \tag{2}$$

Thus, in order to determine the charge carrier concentrations n_e for electrons in the conduction band and n_h for holes in the valence band, the density of available states $D(E)$ of the corresponding band must also be considered. If an electron is lifted from the valence to the conduction band, a corresponding hole in the valence band must have been created, so that

$$n_\mathrm{e} = n_\mathrm{h} \ . \tag{3}$$

The charge carrier concentrations of electrons n_e and holes n_h can then be described by

$$n_\mathrm{e} = \int_{E_\mathrm{C}}^{+\infty} f(E) \cdot D(E)_\mathrm{CB}\ dE \approx N_\mathrm{C} \exp\left(-\frac{E_\mathrm{C} - E_\mathrm{F}}{kT}\right) \tag{4}$$

$$n_\mathrm{h} = \int_{-\infty}^{E_\mathrm{V}} (1 - f(E)) \cdot D(E)_\mathrm{VB}\ dE \approx N_\mathrm{V} \exp\left(-\frac{E_\mathrm{F} - E_\mathrm{V}}{kT}\right) \tag{5}$$

where N_C and N_V describe the effective density of states in the conduction and valence band respectively. The product of the two charge carrier concentration in equilibrium is according to

$$\begin{aligned} n_\mathrm{i}^2 &= n_\mathrm{e} \cdot n_\mathrm{h} \\ &= N_\mathrm{C} \exp\left(-\frac{E_\mathrm{C} - E_\mathrm{F}}{kT}\right) \cdot N_\mathrm{V} \exp\left(-\frac{E_\mathrm{F} - E_\mathrm{V}}{kT}\right) \\ &= N_\mathrm{C} N_\mathrm{V} \exp\left(-\frac{E_\mathrm{C} - E_\mathrm{V}}{kT}\right) \\ &= N_\mathrm{C} N_\mathrm{V} \exp\left(-\frac{E_\mathrm{G}}{kT}\right) \end{aligned} \tag{6}$$

independent from the Fermi energy and therefore independent of the doping. [12, 11]

The Fermi-level and Electrochemical Potential Keeping in mind the condition for intrinsic semiconductors in equilibrium, that the product of the charge carrier con-

centration for both holes and electrons remains the same, the position of the Fermi-Level for an intrinsic semiconductor is then determined by 4 and 5 to

$$E_{\mathrm{F}} = \frac{1}{2}\left(E_{\mathrm{V}} + E_{\mathrm{C}}\right) + \frac{1}{2}kT \ln \frac{N_{\mathrm{V}}}{N_{\mathrm{C}}} \tag{7}$$

[12]

Doping in Semiconductors Especially in solar cell physics, the doping of semiconductors plays an important role. Hereby, donor or acceptor atoms are inserted in the intrinsic semiconductor to produce a higher concentration of electrons or holes respectively. Donors D offer an energy level close to the conduction band minimum (CBM), so that it needs less energy to lift an electron to the conduction band $\mathrm{e}^-_{\mathrm{CB}}$, which then leaves a positive charged donor ion D^+ behind according to

$$\mathrm{D} \longrightarrow \mathrm{D}^+ + \mathrm{e}^-_{\mathrm{CB}} \,. \tag{8}$$

This leads to an increase of electron concentration in the conduction band.
Acceptors A offer an energy level close to the valence band maximum (VBM), so that it needs less energy to extract an electron from the valence band, which leads to a negative charged acceptor ion A^- and a hole left behind in the valence band $\mathrm{h}^+_{\mathrm{VB}}$ according to

$$\mathrm{A} \longrightarrow \mathrm{A}^- + \mathrm{h}^+_{\mathrm{VB}} \,. \tag{9}$$

The insertion of acceptor atoms leads to an increase of the hole concentration inside the valence band.
Doping with donors or acceptors and their unilateral influence on the charge carrier concentrations causes a shift of the Fermi-level towards the CBM or the VBM respectively, what can be seen in figure 2. The increased electron concentration in the conduction band is the reason why doping with donors makes a semiconductor an electron conductor (n-type or n-doped) whereas doping with acceptors makes it a hole conductor (p-type or p-doped) due to increased hole concentration in the valence band. The prevailing charge carriers are called majority carriers (electrons for n-type and holes for p-type semiconductors) and the respective other minority carriers.

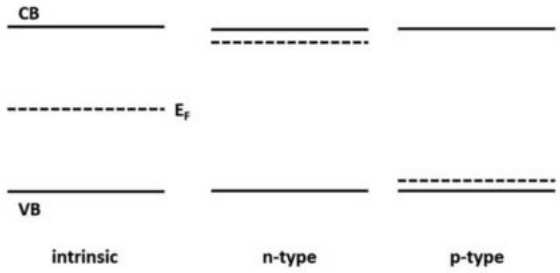

Figure 2: Illustration of the different relative positions of the Fermi level inside the band gap for intrinsic, n-type and p-type semiconductors. For an intrinsic semiconductor, the Fermi level is located approximately in the middle of the band gap, whereas n-doping leads to a shift towards the CBM and a p-doping towards the VBM. Taken from [13]

At room temperature, the energy is sufficient for the electrons to overcome the gap between the donor or acceptor level and the corresponding band edge, so that all donor or acceptor atoms are ionized and the charge carrier concentration equals the donor or acceptor concentration n_D and n_A respectively, according to

$$n_\mathrm{e} \approx n_\mathrm{D} \tag{10}$$

$$n_\mathrm{h} \approx n_\mathrm{A} \ . \tag{11}$$

This information can be used to determine the new Fermi-levels based on 7 and solving it for the Fermi-level in an n-type semiconductor to

$$E_\mathrm{F,n} = E_\mathrm{C} - kT \ \ln \frac{N_\mathrm{C}}{n_\mathrm{D}} \tag{12}$$

and for a p-type semiconductor to

$$E_\mathrm{F,p} = E_\mathrm{V} + kT \ \ln \frac{N_\mathrm{V}}{n_\mathrm{A}} \ . \tag{13}$$

To complete the section about doping in semiconductors it must be mentioned that the doping itself does not influence the square of the intrinsic charge carrier concentration n_i^2 as equation 6 is still valid due to shifting of the Fermi-level.

A summary of the different semiconductor types (intrinsic, n-type, p-type) and their characteristic charge carrier related parameters can be seen in table 1.

Table 1: Summary of different parameter definitions for the three semiconductor types intrinsic, n-type and p-type, modified according to [12].

type	$n_{\mathbf{e}}$	$n_{\mathbf{h}}$	$E_{\mathbf{F}}$
intrinsic	$N_{\mathrm{C}} \exp\left(-\frac{E_{\mathrm{C}}-E_{\mathrm{F}}}{kT}\right)$	$N_{\mathrm{V}} \exp\left(-\frac{E_{\mathrm{F}}-E_{\mathrm{V}}}{kT}\right)$	$\frac{1}{2}\left(E_{\mathrm{V}}-E_{\mathrm{C}}\right)+\frac{1}{2}kT\ln\frac{N_{\mathrm{V}}}{N_{\mathrm{C}}}$
n-type	n_{D}	$\frac{n_{\mathrm{i}}^2}{n_{\mathrm{e}}}=\frac{n_{\mathrm{i}}^2}{n_{\mathrm{D}}}$	$E_{\mathrm{C}}-kT\ln\frac{N_{\mathrm{C}}}{n_{\mathrm{D}}}$
p-type	$\frac{n_{\mathrm{i}}^2}{n_{\mathrm{h}}}=\frac{n_{\mathrm{i}}^2}{n_{\mathrm{A}}}$	n_{A}	$E_{\mathrm{V}}+kT\ln\frac{N_{\mathrm{V}}}{n_{\mathrm{A}}}$

2.1.3 Photoabsorption - Charge Carriers in Non-equilibrium

So far, only the charge carrier conditions in equilibrium have been considered. In order to obtain free charge carriers for solar energy conversion, the processes that take place under irradiation, or in non-equilibrium, are particularly relevant. When a semiconductor absorbs a photon with sufficient energy, there is a transfer of energy from the photon to the electron so that it is lifted from the valence band to the conduction band. It leaves behind an electron vacancy, i.e. a hole. Therefore, photoabsorption results in a higher concentration of both electrons in the conduction band and holes in the valence band, and thus both the electron and hole concentrations within the corresponding bands increase in comparison to the equilibrium.

As a consequence of the increased electron concentration in the conduction band, the Fermi level shifts towards the conduction band, whereby at the same time a shift towards the valence band would be expected due to the increased hole concentration in the valence band. The consequence of this is the separate description of the Fermi-levels for electrons $E_{\mathrm{F,C}}$ and holes $E_{\mathrm{F,V}}$. This difference in the Fermi distributions of electrons and holes in non-equilibrium is called quasi fermi level spitting. The charge carrier concentrations are now described as

$$n_{\mathrm{e}} = N_{\mathrm{C}} \exp\left(\frac{E_{\mathrm{C}} - E_{\mathrm{FC}}}{kT}\right) \tag{14}$$

$$n_{\mathrm{h}} = N_{\mathrm{V}} \exp\left(\frac{E_{\mathrm{FV}} - E_{\mathrm{V}}}{kT}\right) \ , \tag{15}$$

which results in the fact that their product is now greater than the square of the intrinsic concentration $n_{\mathrm{i}}^2 < n_{\mathrm{e}} \cdot n_{\mathrm{h}}$ with

$$\begin{aligned} n_{\mathrm{e}} n_{\mathrm{h}} &= N_{\mathrm{C}} N_{\mathrm{V}} \exp\left(\frac{E_{\mathrm{FV}} - E_{\mathrm{V}}}{kT}\right) \exp\left(\frac{E_{\mathrm{FV}} - E_{\mathrm{V}}}{kT}\right) \\ &= n_{\mathrm{i}}^2 \exp\left(\frac{E_{\mathrm{FC}} - E_{\mathrm{FV}}}{kT}\right) \ . \end{aligned} \tag{16}$$

This demonstrates, that in absence of a quasi fermi level splitting, so if $E_{\mathrm{FC}} = E_{\mathrm{FV}}$, the product is only defined by n_{i}^2 as shown in equation 6 which is valid for equilibrium. When there is a quasi fermi level splitting due to photoabsorption, the product is strongly dependent on the amount of the splitting. [12]

2.1.4 Energy Forms of Electrons and Holes

In the previous sections, mainly the charge carrier concentrations in equilibrium and in non-equilibrium for semiconductors have been considered. In order to understand how a current of charge carriers occurs, the energy forms and prevailing potentials, especially the resulting electrochemical potential of electrons and holes are of great importance and will be explained in the following according to [12].

Figure 3 shows the different energy forms for electrons and holes in a semiconductor. For both charge carrier types, the overall electrochemical potential η is built up by the electrostatic potential $-e\varphi$ and the chemical potential μ.

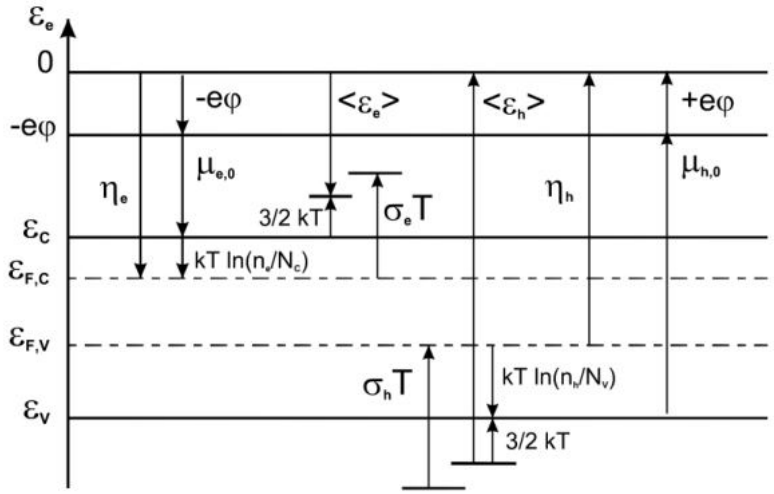

Figure 3: Different energy forms for electrons and holes in a semiconductor. The electrochemical potentials for electrons η_{e} and holes η_{e} are shown, which are divided into the electrostatic and chemical potentials. In addition, the presence of the quasi fermi level splitting shows that this is a semiconductor in non-equilibrium. Taken from [12]

As an example, the electrochemical potential for an electron is given by:

$$\eta_{\mathrm{e}} = -e\varphi - \mu_{\mathrm{e}} \tag{17}$$

whereas the chemical potential of an electron μ_{e} is composed by the material characteristics with the distance from the conduction band edge to the electrostatic potential level and the doping related quantity of the Fermi-level for electrons, which gives the

distance of the Fermi-level to the CBM with $kT \ln\left(\frac{n_e}{N_C}\right)$. The chemical potential of an electron is then

$$\mu_e = \mu_{e,0} + kT \ln\left(\frac{n_e}{N_C}\right) \ . \tag{18}$$

The higher the electron doping concentration, the lower the magnitude of the chemical potential μ_e. In the end, the electrochemical potential for the electron would result in

$$\eta_e = -e\varphi - \mu_{e,0} - kT \ln\left(\frac{n_e}{N_C}\right) \ . \tag{19}$$

2.1.5 Transport Mechanisms of Free Charge Carriers

The reason for using semiconductors for photovoltaic cells or photoelectrochemical water splitting is the ability to generate free charge carriers with a potential difference of the quasi fermi level splitting due to photoabsorption in order to use this energy. For an efficient extraction of the free charge carriers, it is useful to understand the transport mechanisms taking place within the semiconductors. The total driving force for the resulting current inside a semiconductor is the electrochemical potential, which is composed of the electrostatic potential φ and the chemical potential μ. As soon as at least one of these quantities shows a gradient across the material, they act as a force on the charge carriers. Thereby, the gradient of the electrostatic potential $\nabla\varphi(\vec{r}) \neq 0$ causes a field current to equalize charge differences, whereas the chemical potential gradient $\nabla\mu(\vec{r}) \neq 0$ causes a diffusion current to equalize concentration differences. [12]

Figure 4 shows the energy diagram of a semiconductor in equilibrium (no QFL-splitting) with an electrostatic potential gradient $\nabla\varphi \neq 0 = \text{const.}$ forcing electrons to the left side due to a decrease of electrostatic potential from the right to the left side and a chemical potential gradient $\nabla\mu \neq 0 = \text{const.}$ forcing electrons to the right side due to higher electron concentration on the left side. In this case, both resulting currents compensate each other to a total current of zero. [12]

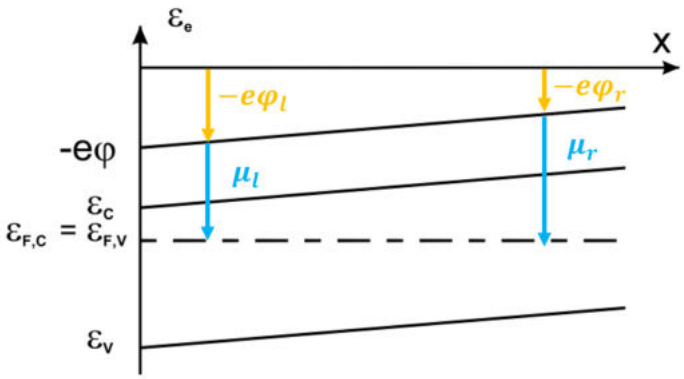

Figure 4: Schematic representation of electron energies in a semiconductor in equilibrium with both electrostatic (orange) and chemical potential gradients (blue) for the left (l) and right (r) side. It can be seen that the electrostatic potential gradient forces electrons to move from the right to the left, whereas the different chemical potentials would force them to the right. The two gradients balance each other out in this example. Modified according to [12]

2.1.6 The Conductivity of Semiconductors

The conductivity σ of a conductor can be described by

$$\sigma = n_\mathrm{e} \mathrm{e} \mu_\mathrm{e}, \tag{20}$$

where n_e describes the electron concentration, e the elementary charge and μ_e the mobility of the electrons. For a semiconductor, hole concentration n_h and mobility μ_h have to be taken into account as well:

$$\sigma = n_\mathrm{e} \mathrm{e} \mu_\mathrm{e} + n_\mathrm{h} \mathrm{e} \mu_\mathrm{h} \tag{21}$$

In an n-type semiconductor, where the electron concentration is significantly higher than the hole concentration, the holes can be neglected and the conductivity of the doped semiconductor becomes again

$$\sigma = n_\mathrm{e} \mathrm{e} \mu_\mathrm{e} \ , \tag{22}$$

whereas for p-type semiconductor the conductivity is mainly determined by the hole concentration and therefore defined by

$$\sigma = n_\mathrm{h} \mathrm{e} \mu_\mathrm{h} \ . \tag{23}$$

[10]

2.2 Semiconductor Junctions

In semiconductor industry and especially for solar conversion devices, a semiconductor is brought into direct contact with the same or different materials to form potential gradients to achieve desired charge carrier flow in a whole cell. The region of the interface is called a junction. In the following, the different classes of junctions that are formed in photoelectrochemical cells are presented.

The main distinction is made between homojunctions and heterojunctions. In homojunctions, the junction is composed of the same materials, but usually with different doping (see section 2.2.1). Heterojunctions, on the other hand, consist of a contact of different materials. These can both be semiconductors with different band gaps (e.g. a-Si/c-Si or Si/Ge) or semiconductors with other material groups like metals. If both junction types occur in a cell, one speaks of hybrid junctions. [14] In addition, there is the semiconductor/electrolyte interface, which is especially important for electrochemical cells or dye-sensitized solar cells.

In the following, the heterojunction semiconductor/metal, the semiconductor/electrolyte interface as well as the p-n-junction (which can consist of a homojunction as well as a heterojunction) including the subform of the tunnel recombination junction will be discussed.

2.2.1 Standard p-n-Junction

The p-n-junction is a very important concept not only for solar energy conversion but also for many electrical devices for example a diode is based on a p-n-junction. P- and n-doped semiconductors are brought into direct contact and can be out of the same materials (p-n-homojunction) or out of materials with different band gaps (p-n-heterojunction). Figure 5 shows the energy diagram of a typical p-n-junction in equilibrium (figure 5a) and in non-equilibrium under illumination (figure 5b). When in contact, the bands of the two materials align according to the different Fermi-levels. The greater chemical potential for electrons on the n-side acts as a driving force for an electron diffusion current from the n- to the p-doped side, where the electron recombines with p-doping induced holes. This results in a relative negative charge inside the p-doped side close to the interface. At the same time, hole diffusion current occurs from the n- to the p-side, what leads to a relative positive charge inside the n-type semiconductor close to the interface. This region, where relative charges occur, is called space-charge-region. Due to a depletion of majority carriers close to the junction, it is also called depletion region. It represents an electrostatic potential acting on the charge carriers inside this region, opposing to the chemical potential gradient. Therefore, the diffusion current continues to flow until the electrostatic potential gradient equals the

chemical potential gradient. The higher the doping concentration inside the semiconductors, the narrower the depletion region because the higher doping concentration leads to increased probability for a diffused charge carrier from the other side of the junction to recombine with a majority charge carrier from the higher doped semiconductor. This can clearly be seen in figure 5a, where the n-doped side on the left has a higher doping level (the Fermi-level is located closer to the CBM on the n-doped side than to the VBM on the p-doped side), and the depletion region, spanned from $-w_n$ to w_p, is narrower than on the p-doped side.

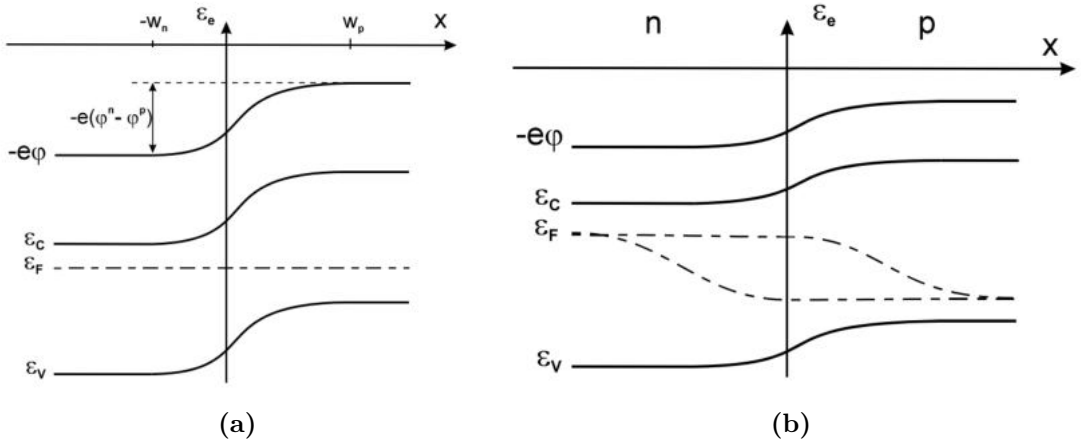

Figure 5: Schematic representation of the energy band diagram in a p-n-junction (a) in equilibrium and (b) in non-equilibrium with quasi fermi level splitting, taken from [12].

However, this also means that the doping concentrations of the two sides for the p-n junction determine the chemical potential gradient, which drives the diffusion current and the electrostatic potential gradient, which drives the drift current. When no external voltage is applied, the electrostatic potential difference $\varphi^n - \varphi^p$, is given by

$$\varphi^n - \varphi^p = \frac{kT}{e} \ln \frac{n_\mathrm{D} n_\mathrm{A}}{n_\mathrm{i}^2} \tag{24}$$

This potential difference is caused as a reaction to the chemical potential gradient. In equilibrium, the electrostatic potential gradient extincts the chemical potential gradient. Thus, the charge carriers do not experience any forces. [12]

Figure 5b shows the p-n-junction in non-equilibrium, so under illumination. The generation of additional free charge carriers via photoabsorption leads to the Fermi-level splitting, as discussed in section 2.1.3. For an efficient extraction of charge carriers from the p-n-junction, the concentration of the charge carriers, e.g. electrons, should not decrease on their path towards the contacts. This means, that the difference of Fermi-levels on the opposite contact sides of the device $E_{\mathrm{F,left}} - E_{\mathrm{F,right}}$ must not be

smaller than the Fermi-level-splitting $E_{\mathrm{F,C}} - E_{\mathrm{F,V}}$, which is valid for figure 5b. [12] Therefore, the doping concentration (which is equal to the charge carrier concentration in the dark) must be larger than the additional free charge carrier concentration caused by photoabsorption n_{e}^{p} and n_{h}^{n}:

$$n_{\mathrm{D}} n_{\mathrm{A}} \geq n_{\mathrm{e}}^{p} n_{\mathrm{h}}^{n} \tag{25}$$

or expressed in energy form

$$kT \ln \frac{n_{\mathrm{D}} n_{\mathrm{A}}}{n_{\mathrm{i}}^{2}} = \mathrm{e}(\varphi_n - \varphi_p) \;\geq\; E_{\mathrm{F,C}} - E_{\mathrm{F,V}} = kT \ln \frac{n_{\mathrm{e}}^{p} n_{\mathrm{h}}^{n}}{n_{\mathrm{i}}^{2}} \tag{26}$$

This means that the electrostatic potential difference of a p-n-junction in the dark must be at least as large as the fermi level splitting due to illumination of this junction.

2.2.2 Tunnel Recombination Junctions

A tunnel recombination junction (TRJ) is a p-n-junction with very high doping concentrations. As a consequence, the energy levels of the p-doped materials VBM and the n-doped materials CBM approach. Ideally, the energy level of the CBM even exceeds that of the CBM due to the Fermi-levels lying inside the bands. As the energetic distance of the bands at the interface decreases, the depletion region of the p-n junction also decreases. Bringing the two band edges closer together enables a charge carrier recombination from electrons of the CBM with holes from the VBM. The fundamental concept behind this is quantum tunneling, which will be explained in this section.

Physics of Quantum Tunneling The principle of a tunnel recombination junction is based on quantum tunneling: The probability to find an electron at a certain location $|\Psi|^2$ is given by the square of its wavefunction Ψ that has to fulfill the Schrödinger-equation

$$-\frac{\hbar^2}{2m}\frac{d^2\psi}{dx^2} + V\psi = E\psi \tag{27}$$

with $\hbar$ being the reduced Planck constant, ψ the wave function of the particle, x the location of the particle, m its mass, E its kinetic energy and V the potential energy [15, 11]. The principle of quantum tunneling is simplified shown in figure 6. When a particle with a kinetic energy of E and an incident wave function Ψ_{incident} moves on the x-axis from the left to the right, it approaches a potential barrier $E_0 > E$, shown in blue.

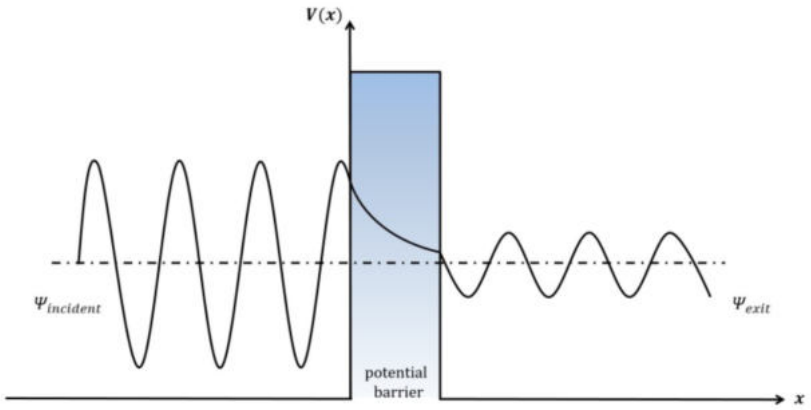

Figure 6: Schematic representation of quantum tunneling. It can be seen how the amplitude of the particle's wavefunction decreases exponentially inside the barrier when travelling from the left to the right. As a consequence, the exit wavefunction on the right side is not zero. Taken from [16]

From classical mechanics one knows, that a particle with less kinetic energy could not overcome a potential barrier with $E_0 > E$. The particle would be reflected completely. For quantum particles, the amplitude of their wavefunctions decreases exponentially inside the barrier. As a consequence, the wave function on the other side of the barrier Ψ_{exit} is not zero, what means that there is a solution for the Schrödinger equation and there is a probability for transmission to the other side, in contrast to classical mechanics [11]. This process is called quantum tunneling. The tunnel probability is highly correlated with the energy and width of the barrier [17].

Tunnel Recombination Junctions in Tandem Devices Especially in solar energy conversion, the concept of using two semiconductors in direct contact plays an important role [18], e.g. to use different wavelength ranges of the solar spectrum with different band gaps for photovoltaic devices or to deliver the required voltage for solar water splitting. Tunnel recombination junctions are used to connect the subcells physically and electrically in series to enable the recombination of free majority-carriers from each cell [19]. The phenomenon of interband tunneling at the interface of a p- and an n-doped material was discovered by Esaki in 1958 [20] when he was studying p- and n-doped Germanium layers. Figure 7 shows his schematic representation of the energy bands of a tunnel recombination junction.

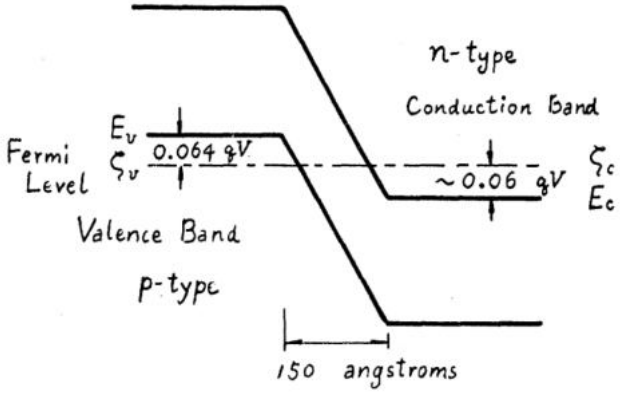

Figure 7: Schematic sketch of a tunnel recombination junction energy band diagram from Esaki in 1958 [20].

The band edges of the p-type material are shown on the left side, the ones from the n-type material on the right side. The VBM as E_V and the CBM is marked as E_C. The Fermi-level is shown as a dashed line with ζ_V for the Fermi-level inside the p-doped material and ζ_C inside the n-type material. The depletion region is said to be about 150 Angstroms. In the figure it can be seen that both materials are heavily doped so that the Fermi-level is found to be inside the valence band for the p-doped and inside the conduction band for the n-doped material. This is the reason for the narrow depletion region, which in turn leads to an increased probability for tunneling of electrons from the valence band of the p-doped material into the conduction band of the n-doped material.

Especially in tandem devices, the TRJ between the subcells plays an important role regarding efficient charge collection as it influences the overall tandem performance due to affection of the short-circuit current density, the fill factor and the open-circuit voltage [19]. Tandem devices with TRJ can be found in the literature especially for solar cells with the tunable band gap material perovskite [21, 22, 23]. Jost et al. [24] for example could improve the efficiency of a CIGSe/perovskite tandem device from 3.1 to 18.2 % by changing the recombination interface materials. However, the implementation of a TRJ in tandem devices is more complicated than for an ideal Esaki-diode: Often, different semiconductor materials require the implementation of the TRJ in a heterojunction with Fermi-levels lying inside the band gaps. Therefore, the tunnel junctions, especially with perovskite solar cells, are often not ideal Esaki-diodes. [19]

Figure 8 shows the band diagram of a Si/perovskite tandem solar cell studied by Rolland et al. in 2018 [22].

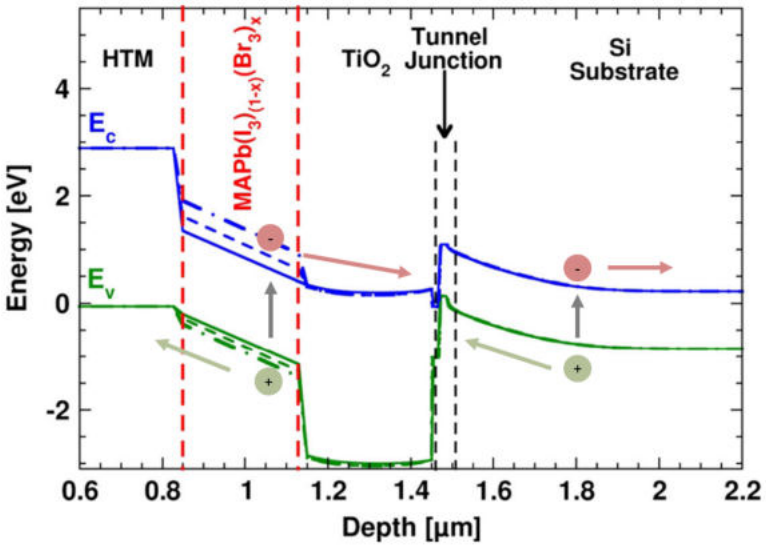

Figure 8: Schematic representation of the energy band diagram of a Si/perovskite tandem solar cell with tunnel recombination junction, marked between the TiO_2 electron transport layer and the Si substrate. [22]

This Si/perovskite tandem cell is made up by a hole transport material (HTM), the perovskite absorber (marked in red), a TiO_2 electron transport layer and a-Si(n^{++})/Si(p^{++}) tunnel junction on a Silicon substrate (the $^{++}$ indicates high doping concentrations). If free charge carriers are created by photoabsorption in the two cells, electrons will travel to the Si substrate and will be collected via an electron contact and holes will travel to the HTM and will be collected by a hole contact. As both TiO_2 and the Silicon substrate are n-type semiconductors, their Fermi-level is located close to the CBM. A direct contact would therefore result in a high potential barrier for electrons when they travel from the perovskite to the silicon layer. [22]

2.2.3 Semiconductor Metal Junction

The metal contact of solar energy conversion devices is intended to facilitate charge carrier transport between the cell and a load. The band alignment at contacting behaves similarly to a semiconductor-semiconductor contact. [12]

The chemical potential of the metal is given by the chemical potential of the electrons $\mu_{e,m}$. When contact is made with a semiconductor, an electrochemical potential gradient occurs, which is balanced by a diffusion current. This results in a contact potential difference until an electronic equilibrium is established. [12, 13]

The total electric potential difference of the space charge region drops within the semiconductors close to the metal interface. Depending on the doping of the semiconductor and the relative position of the work function of the metal, there is an accumulation or

depletion of majority charge carriers (electrons in n-type and holes in p-type semiconductors) in the space charge region. An accumulation is called an ohmic contact and a depletion is called a Schottky contact. [12]

Figure 9 shows the different metal-semiconductor contacts that can be created.

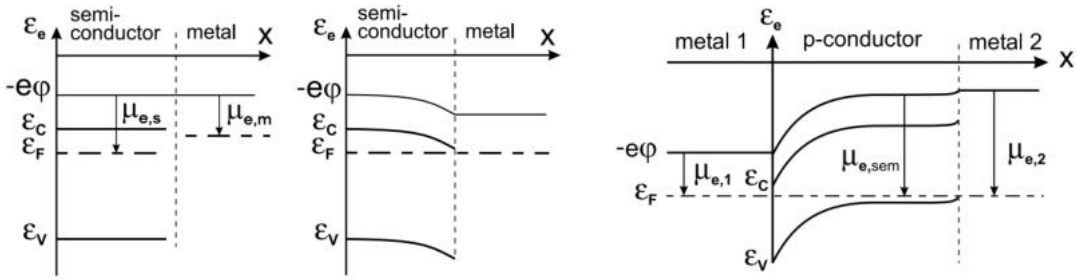

(a) Ohmic contact **(b)** Both Schottky and ohmic contact.

Figure 9: Schematic representation of the energy band diagrams for ohmic and Schottky metal-semiconductor contacts. a) shows the ohmic contact of an n-type semiconductor and a low work function metal. On the other side, both contact types are shown in b). A p-doped semiconductor is brought into contact with metal 1 with a small work function on the left side and with metal 2 with a large work function on the right side, resulting in a Schottky contact on the left and an ohmic contact on the right. Taken from [12]

Figure 9a shows a semiconductor-metal junction with an n-type semiconductor and a metal with lower work function than the semiconductor. The band diagram before and after contacting is shown. Before contacting, it can be seen that the magnitude of the chemical potential from the metal $\mu_{\mathrm{e,m}}$ is smaller than that of the chemical potential of the electrons of the semiconductors $\mu_{\mathrm{e,m}}$, resulting in a chemical potential gradient from the metal to the semiconductor. This causes electrons to diffuse from the metal to the semiconductor upon contacting due to this chemical potential gradient. This results in band bending with an accumulation of electrons and thus a region of negative space charge near the surface of the semiconductor. In figure9b a p-type semiconductor is shown in contact with a high work function metal on the right and a low work function metal on the left. [12]

2.2.4 Semiconductor Electrolyte Interface

When semiconductor and electrolyte are in contact, the charge carrier balance behaves similarly to metal and semiconductor. The redox Fermi-level $E_{\mathrm{F,redox}}$ plays the same role as the Fermi-level of semiconductors or metals [25, 13] and is determined by the standard chemical potentials of the reducing and oxidizing species (μ^0_{R} and μ^0_{O}) and

their concentrations (N_R and N_O):

$$E_{\mathrm{F,redox}} = (\mu_\mathrm{R}^0 - \mu_\mathrm{O}^0) + k_\mathrm{B}T \ln\left(\frac{N_\mathrm{R}}{N_\mathrm{O}}\right) . \tag{28}$$

If, for example, an n-type semiconductor is brought into contact with an electrolyte whose chemical potential is greater in magnitude than that of the semiconductor, a depletion of majority charge carriers (in this case electrons) occurs in the semiconductor near the interface, since the chemical potential gradient from the smeiconductor to the electrolyte is balanced. Thus, a region of positive charges (space charge region) is created. On the electrolyte side, an accumulation of negatively charged particles is formed close to the interface, the so-called Helmholtz layer. The width of the space charge region is usually much larger than that of the Helmholtz layer. [13]

2.3 Photoelectrochemical Cells

Photoelectrochemical cells consist of a semiconductor device for photoinduced free charge carrier generation that provides the voltage to drive the water splitting reaction inside an electrolyte that contains the needed ions for the reaction. In this section, general aspects of photoelectrochemical water splitting is explained, followed by the presentation of the working principle of a photoelectrochemical cell. Tandem cells and their limitations are also discussed and it is explained why the use of excess charge carriers by hybrid photoelectrochemical and -voltaic cells can be useful.

2.3.1 Photoelectrochemical Water Splitting

The overall water splitting reaction [13]

$$2\,\mathrm{H_2O(l)} + \mathrm{Energy} \longrightarrow 2\,\mathrm{H_2(g)} + \mathrm{O_2(g)} \quad \Delta G = 237.22\,\mathrm{kJ/mol} \tag{29}$$

with the required Gibbs Free Energy ΔG consists of two half-cell reactions: The hydrogen evolution reaction (HER) with

$$2\,\mathrm{H^+} + 2\,\mathrm{e^-} \longrightarrow \mathrm{H_2} \tag{30}$$

and the oxygen evolution reaction (OER) with [26]

$$2\,\mathrm{OH^-} \longrightarrow \frac{1}{2}\,\mathrm{O_2} + \mathrm{H_2O} + 2\,\mathrm{e^-}. \tag{31}$$

In theory, the Gibbs Free Energy of $\Delta G = 237.22\,\mathrm{kJ/mol}$ corresponds to a required voltage of 1.23 eV (at standard temperature ($T^0 = 298\,\mathrm{K}$) and pressure ($p^0 = 1\,\mathrm{bar}$))

according to

$$U = \frac{\Delta G}{nF} \tag{32}$$

with n being the amount of electrons needed for the reaction (in this case, $n = 2$) and F being the Faraday constant.

The minimum required voltage supplied by a water electrolysis system consists of this 1.23 eV and an the overpotential voltage V_{OP}, which has to balance out losses of the kinetic barriers for the HER η_{A} and OER η_{C} each as well as resistance losses inside the device η_{Ω}. [13]

This required energy can be provided directly by photoelectrolysis, also known as a photoelectrochemical cell.

2.3.2 Working Principle

Figure 10 shows the working principle of a photoelectrochemical cell. An n-type semiconductor is used as a photoanode. It is brought in contact with an electrolyte in which a metal electrode is immersed. The semiconductor is connected to the metal electrode by a conductive substrate and a conductor.

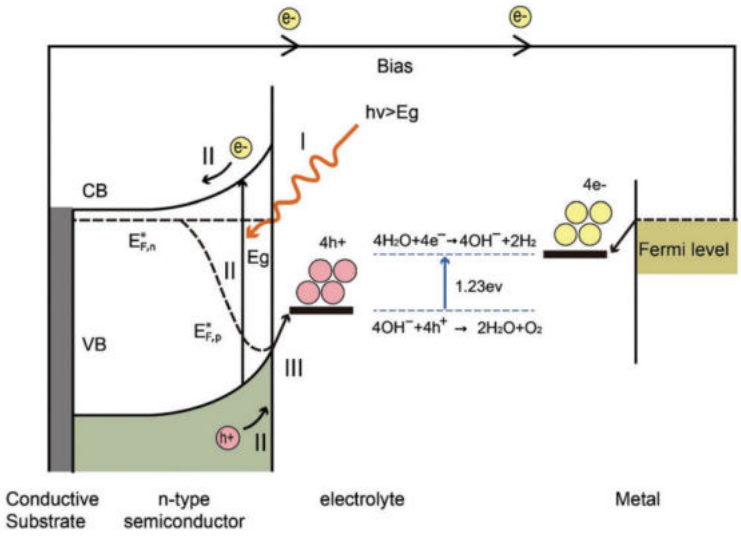

Figure 10: Schematic representation of the working principle of a PEC (taken from [27])

If the cell is now irradiated with light, various processes take place. First, the semiconductor absorbs photons (I) and a Fermi-level splitting occurs within the semiconductors and thus also a charge carrier separation (II). Due to the depletion region and the associated band bending near the interface, the electrons move toward the conductive substrate and the holes move toward the electrolyte. The holes then contribute to

the OER at the semiconductor/electrolyte interface and the electrons, after traveling through the conductor toward the metal electrode, contribute to the HER. It is made clear in the figure, that the photoinduced quasifermi-level splitting provides a voltage greater than the necessary 1.23 eV for the water splitting reaction. [27]

Besides the supplied voltage by the PEC, there are other factors that influence the water splitting ability of a whole cell. For example, surface active sites at the photoanode/electrolyte interface play an important role. In a TiO_2-Photoanode for example, oxygen vacancies, Ti interstitials, and Ti vacancies can lead to higher reactivity with water molecules. [28]

2.3.3 Tandem PEC and its Limitations

Considering the losses that take place inside a PEC, the photoelectrode material should have a band gap of at least 2.03 eV. If a single material provides this band gap, the whole part of the spectrum with lower energy than 2.03 eV will not be used. A tandem configuration with high and lower band gap materials can use the spectrum more efficient. Additionally it can provide enough driving force for self-driven solar water splitting. [18]

However, the overall device current is limited by the material with the lowest current. As long as it cannot be ensured that the same current is generated in the two subcells, the higher current of one material will be limited to the lower current. [12]

2.4 Hybrid Photoelectrochemical- and Voltaic Cells

To overcome this current mismatch, Segev et al. (2018) presented a working hybrid photoelectrochemical and -voltaic cell by integration a TiO_2 photoanode onto an interdigitated back contact (IBC) Si wafer. It uses the excess free charge carriers inside the Si wafer by creating an additional circuit with p-and n-contacts on the back side of the wafer. The cell HPEV cell is shown in figure 11. For the integration they used a fluorine doped tin oxide (FTO) and a p-doped layer. More detailed information on the FTO was not provided. But due to the Fermi level located in the conduction band of FTO, its energy band edges will significantly lower when contacting with TiO_2, whose Fermi level is located close to its conduction band but still inside the band gap. Together with the p^+ doping on the Si wafer, it can be assumed that this is the realization of a TJ.

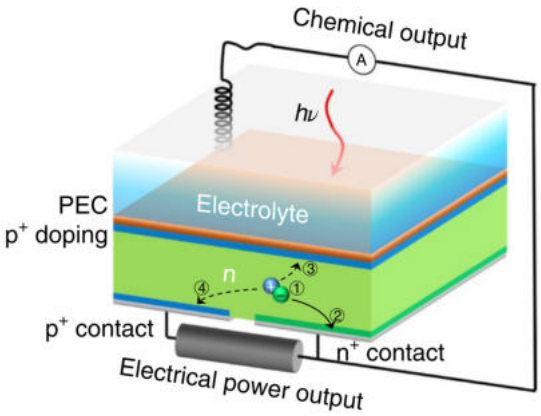

Figure 11: Schematic representation of the working principle of an HPEV cell (taken from [8]).

In figure 11 the photoanode is shown in orange (PEC), the n-type photovoltaic layer in green. The two back contacts (n^+-contact in green and the p^+-contact in blue) are indicated below the PV layer and a p^+-doped layer (blue) above the layer. In addition, the cell consists of an electrolyte, shown here in blue, which is in contact with the photoanode. The cell becomes fully functional due to the metal connection of the n^+ back contact of the PV cell with the cathode that protudes the electrolyte. When irradited with sunlight, both semiconductors absorb photons of the corresponding wavelength. Free electron-hole pairs are generated in both layers. The process within the PV layer is shown schematically in the figure: First, a free electron-hole pair is generated (1). The free hole either migrates to the p-contact on the backside (2), contributing to the electrical power output, or migrates to the p^+-doped layer towards the PEC, contributing here to the increased voltage for chemical output (hydrogen production). In either case, the electron migrates to the n^+ back contact, where it subsequently contributes to either the electrical power or the chemical output.

Segev et al. tested their samples using LSV in the three- and two-electrode configuration with the p^+ back contact disconnected. For the three-electrode configuration, they were able to measure a current density of 1.23 V vs. RHE of $0.104\,\mathrm{mA \cdot cm^{-2}}$. In the two-electrode configuration, a current density of $0.085\,\mathrm{mA \cdot cm^{-2}}$ could be obtained at 0 V vs RHE, i.e., without external bias. [8]

2.5 Semiconductor Materials

In this chapter, the two materials Silicon and TiO_2 together with TiO_x are presented as they act as the main photoabsorbers in the form of a silicon wafer and a TiO_x photoanode in this work.

2.5.1 Silicon

Silicon materials can be divided into amorphous (a-Si) and crystalline silicon (c-Si). Figure 12 shows the different structures. In the crystalline arrangement, each silicone atom forms a bond with four neighboring silicone atoms and assumes the typical tetrahedral shape. In amorphous silicone, on the other hand, the arrangement is more disordered. As a result, some atoms have unsaturated bonds (so-called dangling bonds). By adding hydrogen during production, these dangling bonds can be saturated [29]

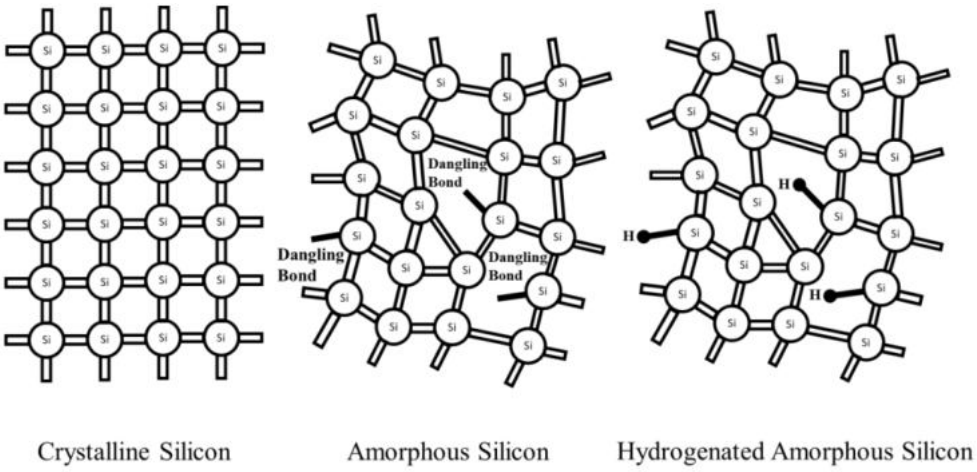

Figure 12: Schematic representation of crystalline and amorphous silicon. Amorphous silicon is shown with dangling bonds and with saturated hydrogenated bonds. Taken from [30]

The two materials differ with respect to their properties, for example, in that a-Si has a higher absorption than c-Si. In addition, the band gap of a-Si is 1.75 eV and that of c-Si is 1.1 eV. [30]

When in contact with air, native oxide of SiO_x grows on a silicon surface [31]. This additional native oxide layer on top of a Silicon structure can be removed by NF_3 etching [32]. Hydrogen passivation can prevent or reduce re-adsorption of ogygen by the saturation of dangling bonds [33]

In this work, the Si wafer used is an n-type crystalline wafer.

2.5.2 TiO_x

TiO_2 is a semiconductor material which is widely used for photoelectrochemical applications [5]. Its band gap with approximately 3 eV [34] suits well for the desired water splitting reaction [6, 5] and has excellent stability against (photo-)corrosion [5]. It can be distinguished between three polymorphs of TiO_2 in nature, that can be used for photoelectrochemical applications. Figure 13 shows the two tetragonal forms with anatase

and rutile and the orthorhombic form brookite. The TiO_6 octahedra are distorted in a different way in a crystal form for every polymorph as can be seen in figure 13. [6]

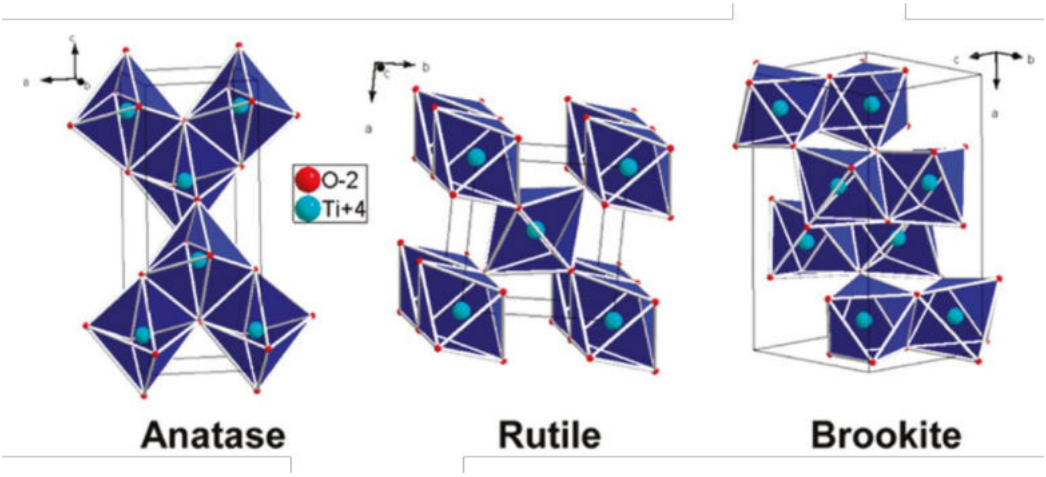

Figure 13: Schematic representation of the different polymorphs of TiO_2 anatase, rutile and brookite. The TiO_6 octahedra are arranged differently in the crystal for each polaymorph [6]

Especially anatase and rutile play an important role for PEC applications. According to Shen et al. [6] bulk rutile has the highest thermodynamic stability whereas anatase is the more active form, probably because of a higher charge carrier mobility. The band gap of antase and rutile is 3.2 eV and 3.0 eV repectively.

The newly developed understochiometric TiO_x Photoanode from Berends et al. is a TiO_2 based Photoanode deposited by reactive magnetron sputtering with bipolar rotary targets. Only titanium is used as target material and oxygen as reactive gas. The power distribution between the two targets is 75 % at one and 25 % at the other target. During the deposition, an oxygen partial pressure of 8 is present. In comparison to a standard TiO_2 material, this results in off-stochiometric samples with an oxygen deficit. A darker material is created that has a higher broad-band absorption coefficient for wavelengths approximately $\lambda > 350$ nm and a higher conductivity. During electrochemical characterization this sample showed the highest performance for solar water splitting and is therefore used in this work. [7]

3 Experimental Methods

3.1 Sample Manufacturing

For the production of the photoelectrode, several layers are required using different deposition methods. The substrate is a commercially aquired unpolished n-doped crystalline silicon wafer, on which the different layers are deposited individually. This subchapter therefore introduces the deposition methods used for this thesis by explaining their basic operation.

3.1.1 Plasma-enhanced Chemical Vapor Deposition

Plasma-enhanced chemical vapor deposition (PECVD) is a type of chemical vapor deposition method. During CVD the film deposition is realized by adding the material precursos in a gaseous and/or vapor form into the chamber. The film deposition is the result of a chemical reaction of the gas inside the chamber. In PECVD technique, the plasma serves to excite the gases by producing radicals based on electron dissociation in order to trigger the chemical reaction. It is caused by a potential in the PECVD chamber. It can therefore take place at lower temperatures than conventional CVD techniques. [35]

The setup of a PECVD chamber can be seen in figure 14. The voltage is applied between the cathode and the grounded electrode, which is placed on a heater. Facing towards the plasma, the substrates are located onto the grounded electrode. Inert and reactive gas flow enable the plasma. The pumps create a vacuum inside the chamber.

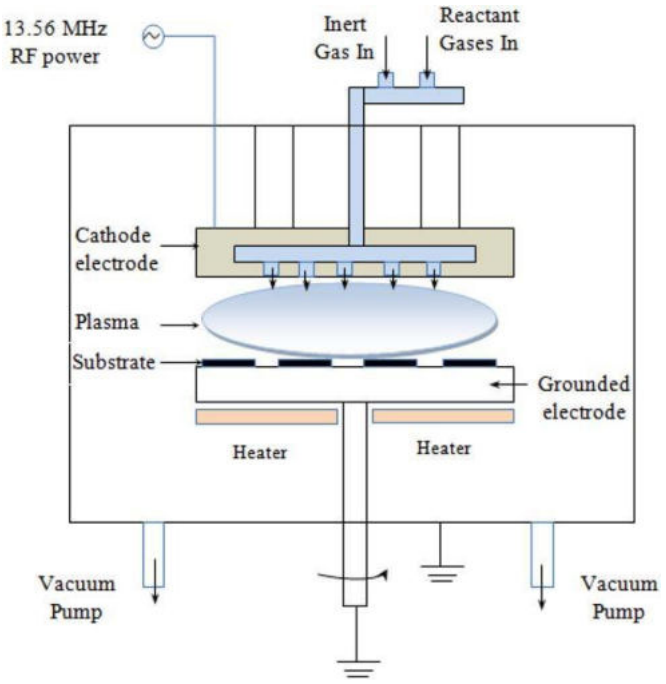

Figure 14: Schematic representation of a plasma-enhanced chemical vapor deposition process. [36]

For thin films based on silicon, monosilane SiH_4 is used as silicon source. Inside the PECVD chamber it dissociates into neutral particles, ions and radicals [37] due to the present plasma. The desired reactions for film formation take place in the whole chamber and condensate on the substrate with

$$SiH_2 \longrightarrow Si_{surf} + H_2 \tag{33}$$

$$SiH_3 \longrightarrow 2\,Si_{surf} + 3\,H_2 \tag{34}$$

where Si_{surf} can occur as amorphous or crystalline phase of Silicon. [38].

In this work, all the PECVD processes are performed with the Cluster tool CS400PS (by *VON ARDENNE GmbH*, Germany). Silane SiH_4 is used as material precursor. For n-doped layers phosphine PH_3 and for p-doped layers diborane B_2H_6 is added to the process as doping gas and phosphorus P or boron B are included as doping atoms inside the silicon films. P-doped and n-doped layers take place at a temperature of 200 °C and 240 °C respectively and are deposited in different chambers.

3.1.2 Physical Vapor Deposition - Reactive Sputtering

In constrast to PECVD the primary source of depositing species during Physical Vapor Deposition (PVD) is solid material, a so called target. The principle of PVD is that atoms are removed from the target, they transit an evacuated chamber and then are deposited on a solid surface where they form a film. There are different ways of removing the atoms from the target, e.g. thermodynamic, with an electron beam or via energetic collision. Latter is called sputtering. [39]
For the deposition of oxides, e.g. TiO_2, sputtering with alternating voltage applied between two targets, is used. This is called bipolar sputtering and avoids accumulation of charges on the surface of the target. The voltage between the cathode and the anode, together with the plasma gas, create the necessary plasma. In reactive sputtering, in addition to the solid target material, a reactive gas is introduced together with the inert gas to form the plasma by the application of the voltage. The reactive gas chemically combines with the sputtered atoms of the target material during film formation. [40]

The probability of plasma particle collision or scattering can be increased by the increase of their path lengths. This can be achieved by increasing the plasma density via applying a magnetic field at the targets through so-called magnetron sputtering. The magnets are placed behind the targets and direct the electrons onto paths in the form of closed loops in order to extend their path lengths. [39]

A schematic representation of the working principle of sputtering is shown in figure 15.

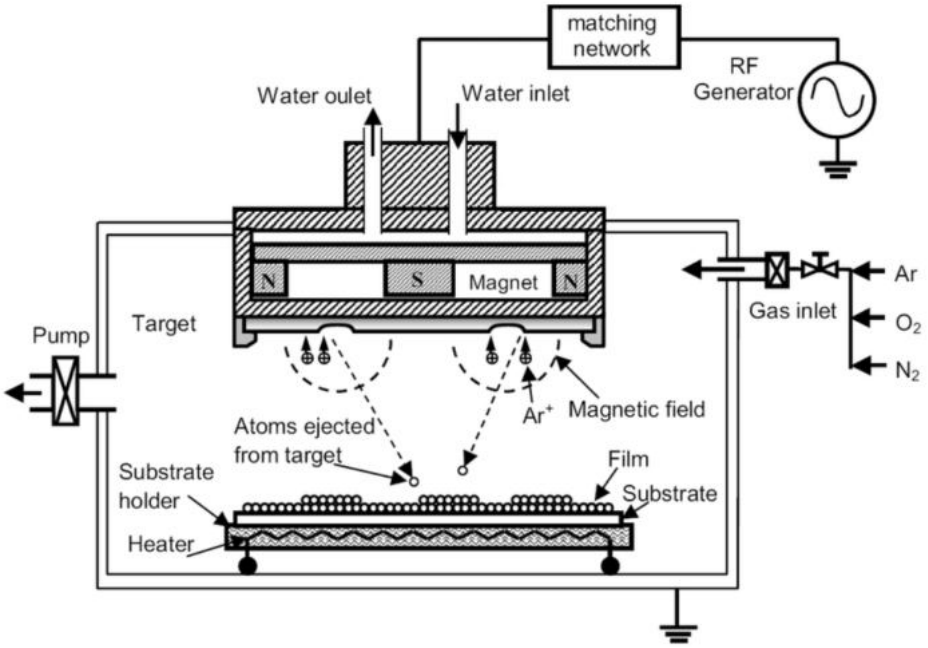

Figure 15: Schematic representation of an RF reactive magnetron sputtering process. The RF generator supplies the electrodes with the corresponding voltage to maintain the plasma. The inert gas Argon is inserted together with the reactive gas O_2. The ionized plasma particles remove particles from the solid target material, which then form a film together with the reactive gas. Vacuum inside the chamber is enabled by pumps. The substrate holder is heated whereas the targets and magnets are cooled with water. Taken from [41].

All sputter depositions referred to this work are carried out with a VISTARIS 600 in-line vacuum System (by *Singulus Technologies AG*, Germany). The same parameters are used during the process that are described by Berends et al [7] for TiO_2 for solar water splitting. Reactive magnetron sputtering is applied. For all processes titanium rotary targets are used as solid target material and O_2 as reactive gas. An oxygen partial pressure of 16e−16 mbar is set and hold during the process. The deposition process is performed bipolar at a present frequency of 50 kHz and a power of 8000 W. Argon with a gas flow of 300 sccm is used as the inert gas. The deposition is performed at a temperature of 200 °C and the sample is preheated 720 s before the deposition is started.

3.1.3 Electron Beam Physical Vapor Deposition

Electron beam physical vapor deposition (EB-PVD) is a form of vapor deposition where the source material is heated in a high vacuum, so that the melting point of the material becomes relatively low. For EB-PVD, an electrom beam generated by a glowing filament is used for heating and is focused on the material via deflection with magnets. The vapor rises as a material steam and then condenses on the substrates that are located on a rotating holder above the crucible with the melted material. Thus a film is formed on the substrates. [40] To control the evaporation process, a shutter is placed between the crucible and the substrates that can block the rising material vapor. In the beginning of the evaporation process, the shutter is closed until a stable process is reached. The deposited film thickness is determined by a piezo element and as soon as the required thickness is reached, the shutter is again closed to protect the substrates from further vapor. All EB-PVD film depositions in this work are performed with the high vacuum deposition electron beam device Dreva Lab 450 (by *Vakuumtechnik Dresden GmbH*, Germany).

3.2 Sample Characterization

In order to be able to evaluate the produced samples, appropriate characterization is essential. In this subsection, the methods used for characterization in this work are presented. First, the characterization methods for the individual layers are presented. These include Raman spectroscopy, Profilometry, UV-Vis spectrometry and dark conductivity and Hall effect measurement. Then, linear sweep voltammetry is described, which is used to characterize the entire PEC electrochemically.

3.2.1 UV-Vis Optical Spectrometry

Important information about the optical properties of materials can be obtained with the aid of UV-Vis optical spectrometry, or in this case UV-Vis-NIR spectrometry. As the name suggests, the instrument can measure in the wavelength range from 200 to 2500 nm, using a deuterium lamp for the 200 to 350 nm range and a tungsten-halogen lamp for the $>$ 350 nm range. A monochromator is located between the light source and the sample in order to select the respective wavelengths and allow them to focus on the sample separately. The transmitted or reflected part of the light is measured by a detector. This is exchanged once at 800 nm, which can lead to increased signal noise in this range.

If transmittance and reflection are known, the absorption coefficient can be determined. This is done on the basis of Lambert-Beer's law for the decrease in intensity of light as

it enters a medium and is taken from [42]:

$$I(x) = I(0) \cdot \exp(-\alpha(\lambda) \cdot x) \tag{35}$$

where $I(x)$ is the light intensity at location x, $I(0)$ is the initial intensity at location $x = 0$ before entering the medium and $\alpha(\lambda)$ is the wavelength dependent absorption coefficient. If the absorption coefficient is to be determined for the entire length $x = d$ (with d as the total penetration depth of the medium), i.e. after the light has exited on the opposite side, the expression $1 - R$ can be used for the initial intensity $I(0)$ and the measured transmittance T can be used for the intensity after exit, so that according to [43] follows

$$\alpha(\lambda) = -\frac{1}{d} \cdot \ln\left(\frac{T}{1-R}\right) \ . \tag{36}$$

Once the spectral distribution of the absorption coefficient is known, the Tauc model can be applied to determine the Tauc-optical-band-gap, which assumes to describe the wavelength-dependent absorption coefficient α as follows:

$$\alpha h\nu = B(h\nu - E_{\mathrm{g}})^{\gamma} \tag{37}$$

Here $h\nu$ represents the energy of the incident photons, B the tauc coefficient and E_{g} the tauc-optical-band-gap. The factor γ depends on the type of electron transition ($\gamma = \frac{1}{2}$ for direct and $\gamma = 2$ for allowed indirect band transition). [44]

Now, if $(\alpha h\nu)^{\frac{1}{\gamma}}$ is plotted over $h\nu$, the tauc-optical-band-gap can be determined via a linear fit to the absorption edge. For spectral characterization of the optical properties, the samples within this work are measured in the Cary 5000 UV-Vis-NIR (by *Agilent Technologies Inc.*, USA). All measurements are baseline corrected and carried out for layers on witness glasses.

3.2.2 Dark Conductivity

The measurement of dark conductivity is of great importance in thin film development, especially of silicone thin films, as it provides information about quantities such as the distance from the Fermi-level to the respective band edge (depending on the doping), room temperature conductivity as well as room temperature resistance and sheet resistance. For the measurement, a voltage is applied to the sample under vacuum between two contacts and the resulting current is measured. The sample is heated up to a certain temperature and then allowed to cool down. This is based on the equation 21 or, for doped layers, on the equations 22 and 23. For simplicity, the procedure is shown

here for an n-doped semiconductor and is taken from [38]. If the electron concentration in equation 22 is replaced by the definition of itself in equation 14, one gets

$$\sigma_{\mathrm{n}} = 2ekT\mu_{\mathrm{e}} \cdot N_{\mathrm{C}} \exp\left(-\frac{\varepsilon_{\mathrm{C}} - \varepsilon_{\mathrm{F}}}{kT}\right) . \tag{38}$$

If the mobility of the charge carriers μ is expressed by the Einstein relation as $\mu_{\mathrm{e}} = \frac{D_{\mathrm{n}}}{kT}$, the general expression of the dark conductivity is as follows

$$\sigma_{\mathrm{dark}}(T) = \sigma_0 \exp\left(-\frac{E_{\mathrm{a}}}{k_B T}\right) , \tag{39}$$

where σ_0 is a prefactor of the conductivity, which is assumed to be temperature independent under the simple model and includes the charge carrier diffusion constant D. E_{a} is the activation energy, which for n-type materials is given by $\varepsilon_{\mathrm{C}} - \varepsilon_{\mathrm{F}}$ and for p-type materials by $\varepsilon_{\mathrm{F}} - \varepsilon_{\mathrm{V}}$. If now equation 39 is logarithmized and plotted against the temperature T in the so-called Arrhenius plot, the activation energy E_{a} can be concluded by a linear fit through the slope, since the logarithmization results in the linear relationship between $\ln \sigma_{\mathrm{dark}}$ and the temperature T

$$\ln(\sigma_{\mathrm{dark}}(T)) = \ln(\sigma_0) + \left(-\frac{E_a}{k_B T}\right) . \tag{40}$$

3.2.3 Hall Effect Measurement

The measurement of the Hall effect is based on the Lorentz force. The principle can be taken from figure 16.

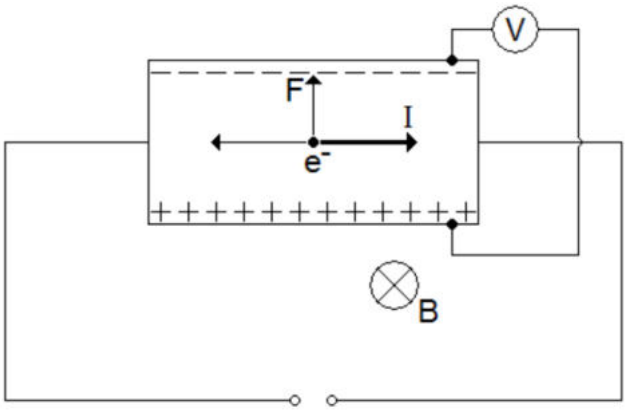

Figure 16: Schematic representation of the principle behind Hall effect measurement of a conductor. The constant current I is indicated to the right inside the sample and the applied magnetic field B points into the image plane. The electrons experience an upward force and are deflected to this sample edge. The charge carriers accumulate and a voltage can be measured between the upper and lower edges. Taken from [45]

The Lorentz force acts on charged particles moving through a conductor in a magnetic field $\vec{B}$ with a velocity $\vec{v}$ perpendicular to these two. In doing so, they experience a force $\vec{F}_{\text{Lorentz}}$, which is normal to the direction of motion and to the magnetic field. This produces an electric field $\vec{E}$, perpendicular to $\vec{v}$ and $\vec{B}$. For a charge q then holds:

$$\vec{F}_{\text{Lorentz}} = q[\vec{E} + (\vec{v} \times \vec{B})] \tag{41}$$

This potential difference between the two sides of the conductor is called the Hall voltage V_{H}. It is defined by

$$|V_{\text{H}}| = \frac{IB}{qn_{\text{s}}} \ , \tag{42}$$

where I is the constant current in the sample and $n_{\text{s}} = nd$ is the sheet density from bulk density n and layer thickness d of charge carriers. Thus, the bulk density can be determined from the Hall measurement with a known layer thickness. If the sheet resistance R_{s} is also known, the charge carrier mobility μ can be determined via [45]

$$\mu = \frac{|V_{\text{H}}|}{R_{\text{s}} IB} = \frac{1}{qn_{\text{s}} R_{\text{s}}} \tag{43}$$

3.2.4 Raman Spectroscopy

Raman spectroscopy can be used to draw conclusions about the composition and crystal structure of sample materials. Monochromatic light generated by a laser with a wavelength of λ_0, is shone onto the sample. With the aid of a monochromator, the radiation scattered by the sample is spectrally decomposed. It can be observed that in addition to the originally irradiated wavelength λ_0 (Rayleigh-scattering), other wavelengths λ_{sc} are present. If $\lambda_{\text{sc}} > \lambda_0$, the photon has transferred energy to the material structure and one speaks of the so-called Stokes radiation. It is determined by the rotational vibration differences of the molecules. However, it can also happen that $\lambda_{\text{sc}} < \lambda_0$, i.e., the energy of the scattered light is greater than that of the incident light. This so-called anti-Stokes radiation occurs when molecules that have already been excited are excited again and now enter a lower energy state.

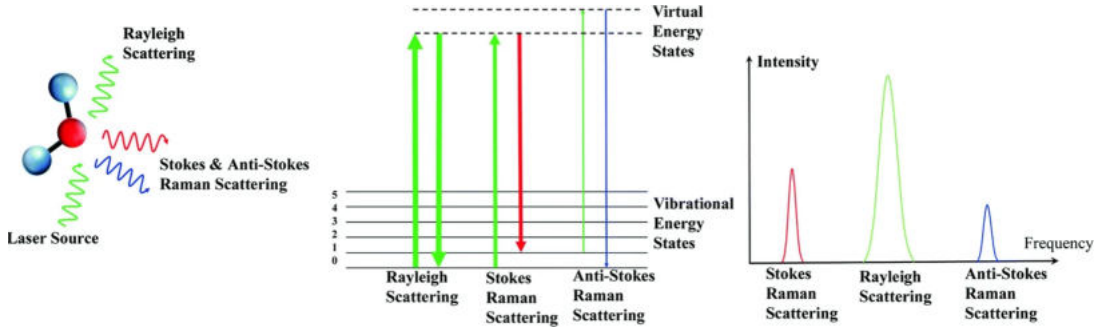

Figure 17: Principle of different molecule scattering forms inclusive Raman scattering. As incident laser source, a green laser is chosen. As one can see on the left side, the incident light is scattered at the molecule into a green part with the same wavelengths (Rayleigh scattering), into a red part with lower wavelengths (Stokes Raman scattering) and into a blue part with higher wavelengths (Anti-Stokes Raman scattering). The middle part of the figure illustrates the difference in energy of the scattered light for the three scattering processes. On the right, the corresponding measurable Raman intensity is shown for all three scattering processes. Taken from [46]

From the measured frequency shifts of the scattered light, the vibrational frequencies ω_n of the molecules can be determined and, with the aid of knowledge of material-characteristic shifts, allow conclusions to be drawn about the sample under investigation. [11]

Especially for the production of crystalline silicon thin films, the proportion of crystalline to amorphous silicon can be determined via the crystallinity factor X_C. This can be determined from the recorded Raman spectrum of the samples under investigation from the ratio of the areas under the peaks belonging to the respective crystalline and amorphous phases of the silicon. For the deconvolution of crystalline silicon thin films, a peak at 420 - 440 cm^{-1}, 480 cm^{-1}, 504 - 511 cm^{-1} and 514 - 518 cm^{-1} is assigned respectively to the longitudinal optical (LO), transverse optical (TO) phonon modes of the amorphous phase and the optical vibrational modes of defective and pure Si phase. The crystallinity factor X_C can thus be calculated from

$$X_c = \frac{\sum I_c}{\sum I_c + \eta \sum I_a} \tag{44}$$

where $\sum I_c$ represents the integrated intensities of the peaks emanating from the crystalline phase (i.e. 504 - 511 cm^{-1} and 514 - 518 cm^{-1}), I_a represent the integrated intensities peaks emanating from the amorphous phases (i.e. 420 - 440 cm^{-1} and 480 cm^{-1}). η was chosen to be 0.8. [47] In figure 18 the deconvolution is shown on an example of a ca. 20 nm nc-Si:H film.

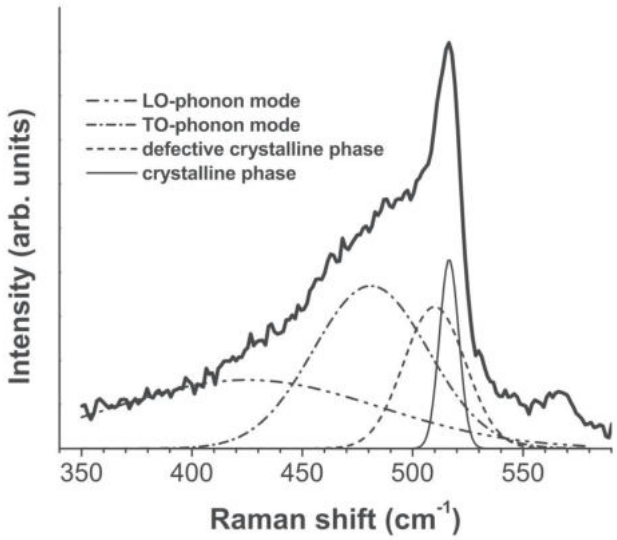

Figure 18: Example plot for deconvolution of Raman spectrum for determination of silicon crystallinity [47].

The measured data is shown as a solid black line. Underneath the contributions of the amorphous and crystalline phases are shown.

For the deconvolution, the three measured Raman spectra are averaged and baseline corrected manually. Gaussian curves are fitted to this curve using a multiple peak fit. The curves are fitted by

$$y = y_0 + \frac{A}{w\sqrt{\pi/2}} \exp^{-2\frac{(x-x_C)^2}{w^2}} \tag{45}$$

to the data (here x,y) and give the results for the offset y_0, the area A, the width w, and the center of the peaks x_C including errors. The overall fit is a cumulative fit.

All samples in this work are measured with a laser of 488 nm using a Senterra System (by *Bruker Corporation*, USA) and the deconvolution is performed with OriginLab [48].

3.2.5 Profilometer

The thickness of the single layers are measured with a profilometer. Before deposition, the glass substrates are marked with a pen marker. After deposition the pen color is removed with isopropanol to expose the layer edge. A diamond pin can then measure the thickness via moving orthogonal to the layer edge. The pin uses a certain force to press on the surface and can therefore recognize height variations of 0.1 nm. Profilometry measurements are performed with the DektakXT stylus profilometer (by *Bruker Corporation*, USA).

3.2.6 Linear Sweep Voltammetry

For the electrochemical characterization of the PECs, linear sweep voltammetry (LSV) is performed. Figure 19 shows the schematic setup of an LSV measurement on a PEC. A voltage is applied and subsequently increased between the Si wafer bottom cell (working electrode) and the platin wire inside the electrolyte (counter electrode). The resulting current is measured.

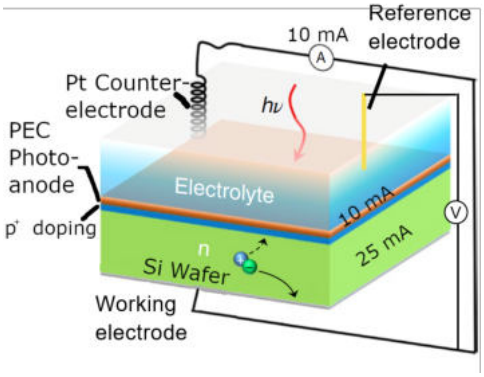

Figure 19: Experimental setup for linear sweep voltammetry as schematic representation, modified according to [8]. The working electrode is connected to the back contact and the counter electrode to the platin wire. The reference electrode protrudes into the electrolyte from above.

The voltage is given as potential with respect to a reference electrode, which also protrudes into the electrolyte. It is applied between the reference and the working electrode and causes a potential between the working and the counter electrode. After light absorption and successful charge carrier separation, electrons would then flow from the working to the counter electrode into the electrolyte where the HER and OER take place.

In figure 20 an example plot of the linear sweep voltammetry measurement result of a $BiVO_4$ can be seen. Besides the dark measurement curve, the light measurement is differentiated between an illumination from the back and from the front side. In this work, only front-side illumination is considered.

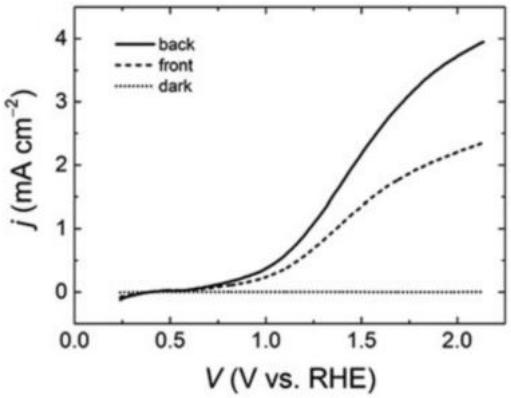

Figure 20: Example of a linear scan voltammetry result for an n-type $BiVO_4$ photoanode, taken from [13]. The current density over the applied potential vs. reversible hydrogen electrode (RHE) for the illuminated sample from the back and front side as well as for the measurement in the dark is shown.

The reason for making both light and dark measurements is to understand the share of the current density coming from absorption and conversion of sunlight, which is called photocurrent density. In consequence, the higher the absorption of a material, the higher should be the difference between dark and light current density. The LSV curve under illumination is characteristic for a PEC. At first, there is hardly any current density, since there is hardly any driving force to successfully separate the charge carriers and mainly recombination of the charge carriers separated by photoabsorption for a short time takes place. If the applied voltage is sufficient, the current density starts to increase. This point is called onset potential and from then on the transfer of charge carriers through the cell increases. [49] If a cell shows a photocurrent at 0 V vs. RHE that suggests that it is suitable for unassisted overall water splitting. [50] However, the dark current density is also important: it can be used to draw conclusions about the stability or possible corrosion of the coatings. If no current can be detected during the dark measurement, this indicates that the coatings are corroded. If a current is detectable, characteristically very small like in figure 20, the materials are stable throughout that voltage range. [13]

All LSV measurements in this work were performed using a VersaSTAT 4 potentiostat (by *Ametek scientific instruments*, USA) and under a halogen lamp of $560\,\mathrm{Wm}^{-2}$ for illumination measurements. During measurement, the voltage is varied between $-0.5-1.7$ V vs. Ag/AgCl at a scan rate of 10 $\frac{\mathrm{mV}}{\mathrm{s}}$. A 3.5 M potassium cloride KCl Ag/AgCl reference electrode and a 0.5 M potassium hydroxide KOH electrolyte is used. For every PEC, three light measurements are followd by three dark measurements. Latter are performed by covering the entire apparatus with a box dyed black from the inside.

For the measurement setup, a 3D printing is used to place the electrolyte on the photoanode and the reference electrode into the electrolyte. Different sizes are used for this. Figure 21 shows both the entire setups and the 3D prints used.

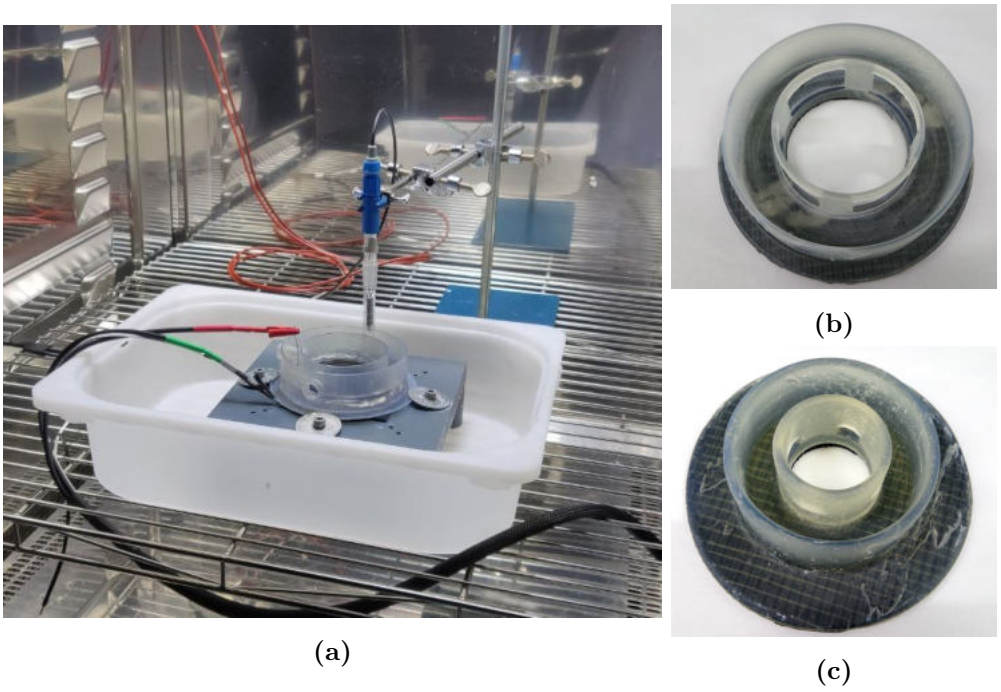

(a) **(b)** **(c)**

Figure 21: Experimental setup design for linear scan voltammetry a) as whole setup with potentiometer connections and the reference electrode. The used 3D-prints to enable the semiconductor/electrolyte interface for a complete PEC show b) the setup for big samples and c) for smaller samples.

The 3D-prints are placed on the samples so that the photoanode faces upwards. The electrolyte is then poured in. By connecting the outer circle with the inner circle via holes, the electrolyte is distributed over both circles. Through the hole facing downwards, the electrolyte in the inner circle is in contact with the photoanode. This thus also determines the active area of the photoanode during a light measurement. The platinum wire is dipped into the electrolyte in the outer circuit. One end protrudes from the electrolyte to connect the potentiometer. The two setups differ mainly the inner holes, by which the smaller setup results in an active area of A_{act} =11.95 cm^2 and the larger one in A_{act} =46.00 cm^2.

4 Interlayer Material Selection

For a successful integration of the photoanode on the silicon wafer, a well-founded material selection for the interlayer is indispensable. This chapter describes the process of material selection by first outlining the requirements placed on the interlayer. Then, various possible materials are presented and the subsequent choice of the material used for this work is justified. Different layer configurations are presented, and their band diagrams are simulated with the help of the Automat FOR Simulation of HETero structures (AFORS-HET) [51].

4.1 Requirements for the Interlayer

To set the requirements for the interlayer, it is first necessary to investigate the properties of the two semiconductor materials (Si wafer and TiO_x photoanode). This allows an analysis of the band alignment without interlayer by means of a simulation of a band diagram.

The properties of the semiconductor materials as used for the simulation can be found in table 2. The value for the band gap of the Si wafer is taken from literature [30] and the one for the TiO_x Photoanode is measured by Dennis Berends (DBS). The remaining data were recorded using Hall effect measurements.

Table 2: Properties of the materials Si wafer and TiOx photoanode used for the band diagram simulation in this work. The negative sign for the bulk electron concentration comes from the negative charge of electrons.

Parameter	**Si wafer**	**TiO_x Photoanode**
Band gap [eV]	1.1 [30]	2.75 [DBS]
Bulk electron concentration [cm^{-3}]	$(-1.52 \pm 0.42) \cdot 10^{15}$	$-3.20 \cdot 10^{23}$
Bulk electron mobility [$\frac{cm^2}{VS}$]	$(9.1 \pm 1.6) \cdot 10^2$	$2.8 \cdot 10^{-4}$

Figure 22 shows the band diagram simulated with AFORS-HET for the case of direct contact of Si wafer and photoanode without an interlayer.

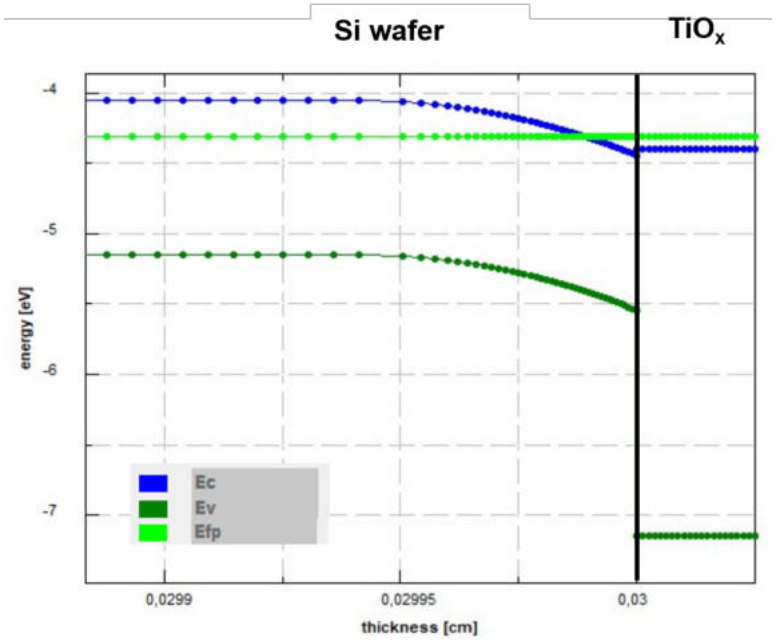

Figure 22: Band diagram of the two semiconductors in direct contact without an interlayer, simulated with AFORS-HET [51]. The VBM (E_V) is shown in dark green, the CBM (E_C) in blue and the Fermi level (E_{fp}) in light green.

In the band diagram, it can be distinguished between the smaller bandgap of silicon on the left and the larger bandgap of TiOx on the right. Since both are n-type semiconductors, the Fermi level of both materials is closer to the respective CBM than to the VBM. However, as identified by the Hall measurements, the carrier concentration of the TiOx with $-3.20 \times 10^{23}\,\mathrm{cm}^{-3}$ is much higher compared to the one of the Si wafer with $-1.52 \times 10^{15}\,\mathrm{cm}^{-3}$ and the distance between Fermi level and CBM is smaller for the photoanode than for the Si wafer, as can be seen from the simulation. The Fermi level of the TiO_x is even within the conduction band in this case. This leads to the fact that in case of a direct contact, the CBM of the photoanode aligns by approx. 0.4 eV below the CBM of the Si wafer. Due to the larger band gap, the VBM of the photoanode is lower by a difference of ca. 2.6 eV below that of the Si wafer.

For the application with TiOx as a photoanode in a PEC, this setup would cause free electrons to migrate from the Si to the TiOx layer and the holes to migrate in the opposite direction when photoabsorption generates free charge carriers within the two materials. From section 2.3 it appears due to redox reaction potential matching, that the holes are required for the OER at the TiOx-electrolyte interface and the electrons must be tapped via the contact at the silicon wafer to contribute to the HER at the platin wire. This would therefore require a flow of electrons from the photoanode into the Si wafer. This is made more difficult by the arrangement without an intermediate

layer due to the band position just described and the resulting high recombination.

To avoid this high recombination, a TRJ can ensure correct current flow. A high p-doping layer has a Fermi-level close to its VBM. Therefore, the use of a p-doping interlayer can provide an energy level close to the CBM of the TiO_x layer. This enables the flow of free electrons in the conduction band from the TiO_x layer towards the Si layer. In the following, possible p-type materials are presented, that have already been used in TRJ.

4.2 P-type TRJ Materials

Wang, Yajie et al. (2018) [52] presented a tunnel recombination junction in a perovskite-CIGS tandem solar cell using aluminium doped zinc oxide (AZO) and nickel oxide (NiO_x). Figure 23 shows the schematic band edges of each layer in the tandem solar cell, indicating the electron movement from the CIGSe layer on the left to the electron contact on the right by the arrows. In addition, the hole movement from the perovskite layer on the right to the hole contact on the left is drawn by arrows, too. The recombination from free charge carriers takes place at the interface between the AZO and the NiO_x layer, where the respective band edges approach.

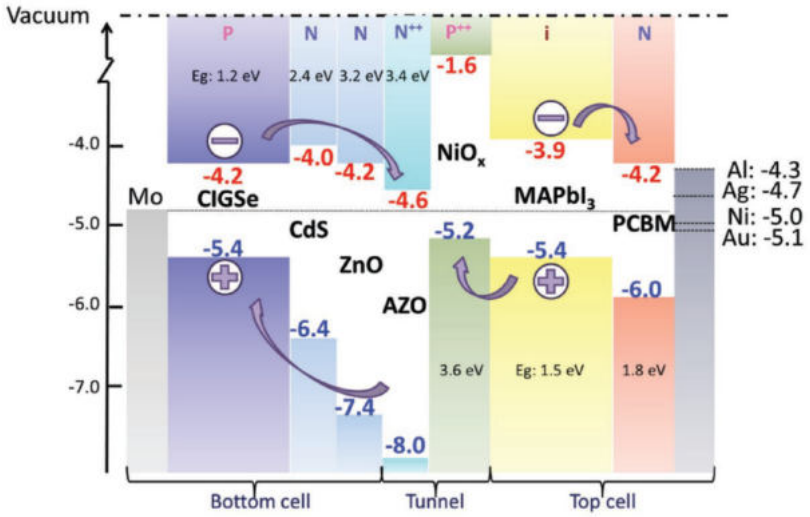

Figure 23: Schematic representation of a TRJ by the location of the energy band edges of each layer in a perovskite CIGS tandem solar cell, taken from [52].

Due to the Fermi level being close to the CBM for AZO (here -4.6 eV) and close to the VBM for NiO_x (here -5.2 eV), a tunnel recombination junction occurs when the two layers contact each other.
The same authors report alternatives to NiO_x. One example of this is MoO_3. Its VBM in their example would beat about -5.3 eV, so even 0.1 eV higher than for NiO_x and

therefore show a higher doping concentration. [52]

Another tunnel junction in a perovskite-Si tandem solar cell was realized by Mailoa et al. in 2015 [21]. They created a silicon tunnel junction between an n-type silicon wafer and a TiO_2 layer integrated in a perovskite-silicon tandem solar cell, which can be seen in Figure 24. The TRJ consists of one highly n-doped amorphous Silicon layer and a p^{++}-type emitter on top of the Si wafer. The n^{++}-doped layer allows the CBM to be lowered enough for electron tunneling into the VBM of the p^{++}-doped layer.

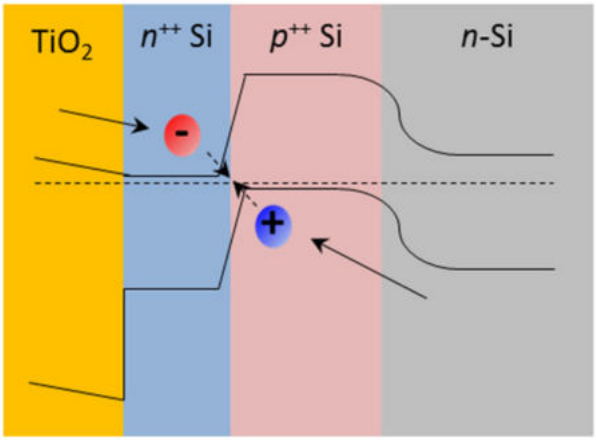

Figure 24: Schematic representation of the TRJ between TiO_2 and an n-type Si layer realized by a n^{++}/p^{++} TRJ, taken from [21].

The TRJ consists of a p-type crystalline emitter on top of the Si wafer and a 30 nm thick n^{++} doped a-Si layer. To reduce possible dopant interdiffusion, a 2-3 nm thick intrinsic a-Si layer was inserted in between. The layers were annealed at 680 °C under N_2 atmosphere. The entire TRJ thus allowed electron transfer from TiO_2 to Si and vice versa for the holes. The charge carrier concentrations inside the a-Si layers were measured to be 10^{19}- $10^{20}\,cm^{-3}$.

4.3 Chosen Material and Sample Setup

Due to the variable doping possibilities and the expertise available in the laboratory, it was decided to use doped crystalline silicon.

Since the Fermi level of the TiO_x lies within the conduction band, the highly n-doped layer from the TRJ as in Mailoa et al. [21] is omitted in this case. Thus, a TRJ is to be realized by adding a single p-doped crystalline silicone layer between the Si wafer and the TiO_x photoanode. The TRJ is then formed between the p-doped crystalline silicon layer with a Fermi-level close to the VBM and the TiO_x photoanode with a Fermi-level

inside the conduction band.

The influence of inserting such a layer on the energy band diagram was studied in AFORS-HET and can be seen in figure 25. Shown are the band diagrams of Si wafer/c-Si(p)/TiO_x in equilibrium. Four different parameter configurations for the film thickness t and the doping concentration N_a for the p-doped Si film are listed. Shown are the CBM (blue), the VBM (dark green), and the Fermi level of the holes (light green). As the band diagrams are shown for the equilibrium, $E_{F,p} = E_{F,n}$.

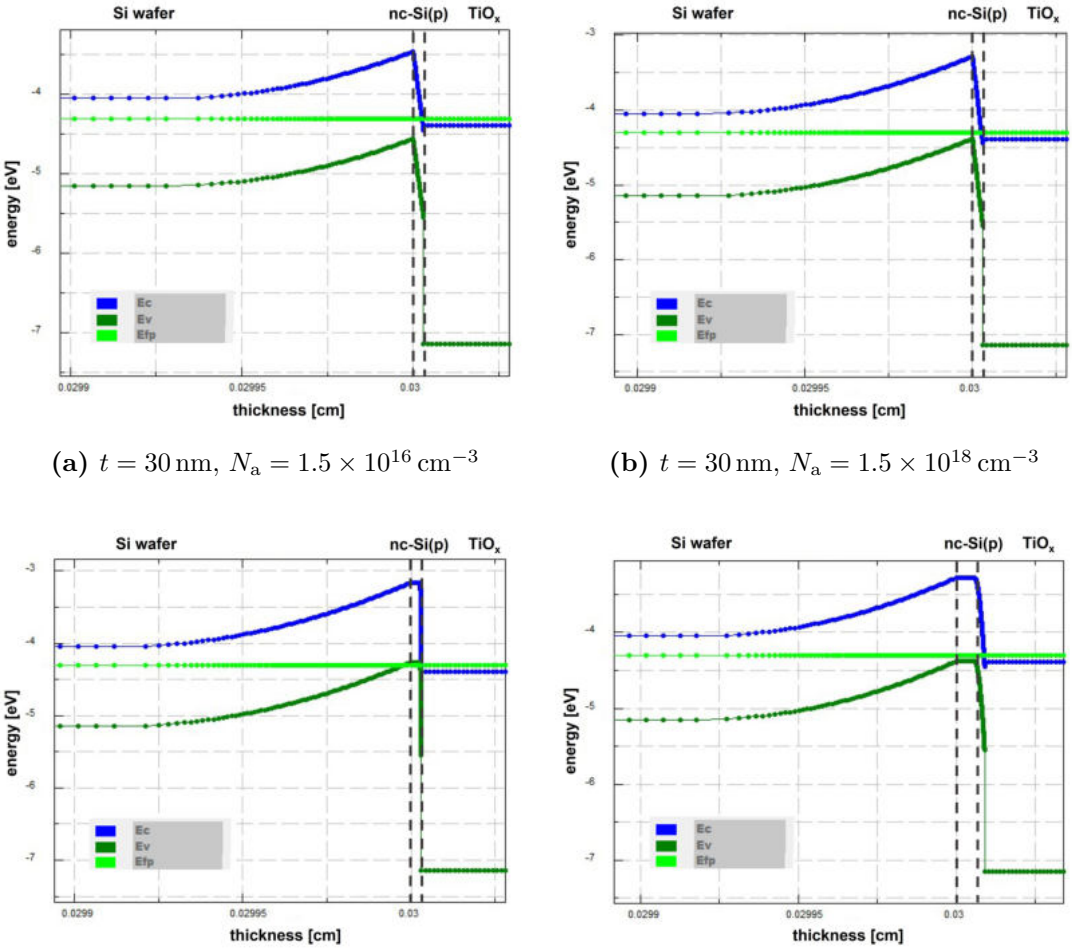

(a) $t = 30\,\text{nm}$, $N_a = 1.5 \times 10^{16}\,\text{cm}^{-3}$ **(b)** $t = 30\,\text{nm}$, $N_a = 1.5 \times 10^{18}\,\text{cm}^{-3}$

(c) $t = 30\,\text{nm}$, $N_a = 1.5 \times 10^{20}\,\text{cm}^{-3}$ **(d)** $t = 90\,\text{nm}$, $N_a = 1.5 \times 10^{18}\,\text{cm}^{-3}$

Figure 25: Band diagrams of c-Si(p) as interlayer between the Si wafer and TiO_x in different parameter configurations, simulated with AFORS-HET [51]. The VBM (E_V) is shown in dark green, the CBM (E_C) in blue and the Fermi level (E_{fp}) in light green.

First, it can be seen for all cases that the addition of the p-doped interlayer results in band bending due to the depletion of majority charge carriers (electrons) in the Si wafer at the interface edge. Therefore, the VBM of the Si wafer is lifted toward the CBM

of the TiO_x layer in the interface region and creates a TRJ. This allows free electrons inside the conduction band of TiO_x to recombine with free holes from the valence band of the Si wafer. For use within a tandem PEC with TiO_x as the photoanode, the holes for the OER are required at the surface of the TiO_x. A flow of electrons from the conduction band from the Si wafer towards TiO_x as in figure 22 in a configuration without TRJ is thus counteracted.

The figure shows the cases for a c-Si(p) film thickness of $t = 30\,\text{nm}$ the ascending doping concentrations from a) $1.5 \times 10^{16}\,\text{cm}^{-3}$ over b) $1.5 \times 10^{18}\,\text{cm}^{-3}$ to c) $1.5 \times 10^{20}\,\text{cm}^{-3}$. Additionally, for the doping concentration of $1.5 \times 10^{18}\,\text{cm}^{-3}$, a distinction is made between the film thicknesses b) 30 nm and d) 90 nm. If the doping concentration increases while the film thickness remains constant (a-c), it can be seen that the energetic distance between the VBM of the Si wafer and the CBM of the TiO_x decreases. This is due to the Fermi level in the c-Si(p) layer moving towards the VBM with increasing doping concentration. For the doping concentrations greater or equal $1.5 \times 10^{18}\,\text{cm}^{-3}$, the VBM of the Si wafer even exceeds the CBM of the TiO_x. For a larger film thickness of 90 nm (d), it can be seen that there is a region with constant band edge positions due to the thicker layer. Here, the position of the Fermi level very close to the VBM can be clearly recognised for the c-Si(p) layer. In further characterization of the layers, the results of the dark conductivity measurements will deliver the activation energy E_a of the layers (Hall measurement, which would deliver the doping concentration, will not be conducted as the layers will be too thin). The aimed activation energy for the c-Si(p) layer should be maximum $E_a \approx 0.1\,\text{eV}$ as indicated by the small distance between the Fermi-level and the VBM in figure 25d.

However, in order to keep the absorption of the c-Si(p) layer as low as possible while enabling tunneling at the junction at the same time, $t = 30\,\text{nm}$ was found to be a promising thickness and is set as the target layer thickness.

After the identification of a material for the realization of a TRJ within the tandem PEC, a proof-of-concept experiment will be performed to find out whether the addition of the TRJ can improve the cell performance in the laboratory.

5 Stack Preparation

In this work, tandem PECs are produced and characterised. The focus is on an intermediate layer between the two absorber layers. In this chapter, the layer stack used with all layers will be presented first, followed by the presentation of the part of the stack that remains unchanged throughout the experiments. For this purpose, the results of the characterizations are presented.

5.1 Sample Stack

A tandem PEC consists of several individual layers. Figure 26 shows the layer stack that was chosen within this work.

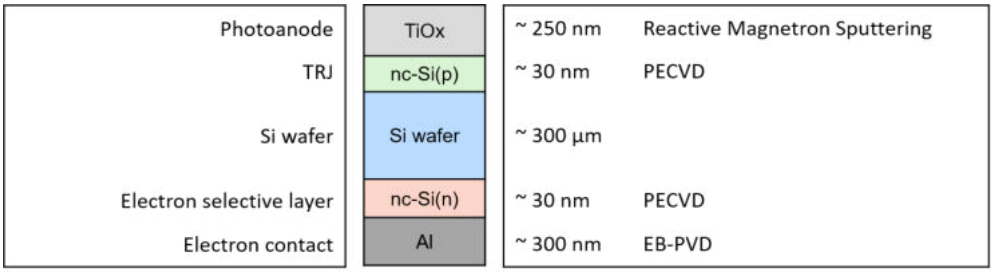

Figure 26: Layer stack as used in this work including approximate layer thicknesses and the corresponding deposition method. The ratios of the layer thickness representation in the center of the figure are for visualization purposes only and do not correspond to the actual ratios.

The substrate material is a purchased n-type crystalline Si wafer, on which nc-Si(n) is first deposited on one side as electron transport layer. This side of the wafer is now referred to as back side. Then c-Si(p) is deposited on the front side. The aluminum back contact is then deposited on the back side. Finally, TiO_x is sputtered onto the c-Si(p) layer.

Since the focus of this work is on the tunnel recombination junction between the c-Si(p) layer and the photoanode, the wafer backside with the c-Si(n) and the Aluminium layer is always coated in the same way and there is no variation of the deposition parameters.

5.2 Wafer Backside

The wafer backside consists of a c-Si(n) layer and an Aluminium layer. Since the manufacturing process of aluminium as electron contact is already established in the laboratory conditions, the characterisation is omitted. Therefore, only the results of the c-Si(n) layer characterization are shown.

5.2.1 Raman Deconvolution

In figure 27, an example deconvolution of the Raman spectrum of a c-Si(n) layer is shown.

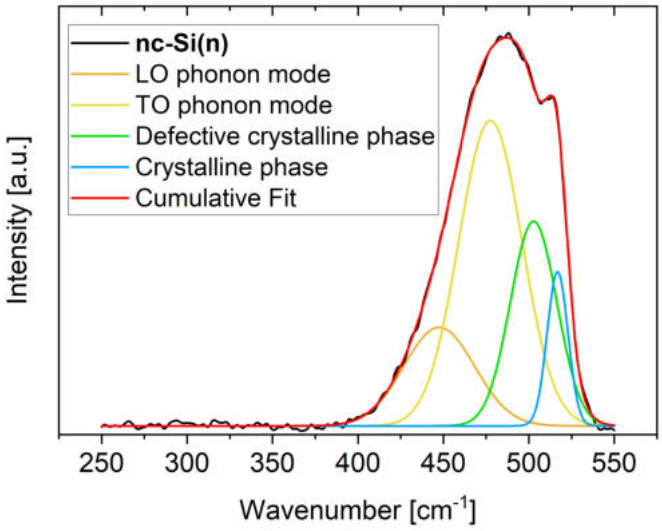

Figure 27: Exemplary Raman signal deconvolution of nc-Si(n) layers. The measured data is given in black. The deconvolution is shown as a cumulative fit (red curve) of the longitudinal optical phonon mode (orange), transversal optical mode (yellow), defective crystalline phase (green) and the crystalline phase (blue) together with the corresponding peak fit centers.

Looking initially only at the measured Raman data, two peaks can be identified, one as a peak tip adjacent to a broader peak. The deconvolution shows that the peak at approx. 520 cm^{-1} comes from the crystalline phase (blue curve) and also from the defective crystalline phase (green curve). The broad peak is composed of the proportions of the amorphous phases (orange, yellow curve). For all deposited c-Si(n) layers a crystallinity factor of $X_C = 0.38 \pm 0.05$ is obtained out of the Raman deconvolution accrording to 44. The peaks of the crystalline phase and a crystallinity factor of 0.38, which is also found in the literature for nc-Si(n) layers in that range [47, 53, 54], confirm that the c-Si(n) layers used in this work are grown as nanocrystalline silicon and they are now referred to as **nc-Si(n)** layers.

5.2.2 Layer Thickness

The nc-Si(n) layers used in this work have a thickness of 29 ± 6 nm. The relatively large standard deviation could have their origin in the process of removing the pen color by the mechanical application of the isopropanol. This mechanical stress, especially around the layer edge, could lead to mechanical removal of the coatings, which varies for different areas. Nevertheless, it can be said that the target thickness of approx.

30 nm was achieved and will also be used in the following for further evaluations.

5.2.3 Tauc Optical Band Gap

Before the results of the individual layers can be evaluated, it must be ensured that the determination of the band gaps from the UV-Vis spectra is carried out below the band gap of the glass substrate. Therefore, figure 28 shows the taucplot for the glass substrate including the determined band gap. Figure 28.

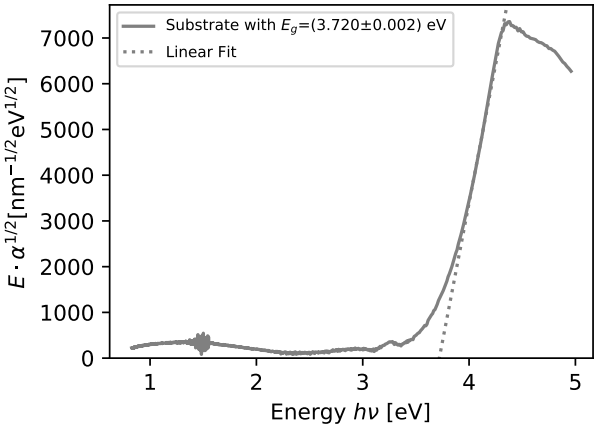

Figure 28: Tauc plot for the glass substrate. The determined band gap is E_g =(3.720 ± 0.002) eV.

It can be seen that the substrate absorbs electromagnetic waves with an energy greater than (3.720±0.002) eV in the energy spectrum.. Thus, it is assumed that the subsequent measurements in this range could be affected by the absorption of the glass. Therefore, the fits for the calculation of the taucplot are only applied for energies $E < 3.720\,\text{eV}$.

Figure 29 shows the exemplary results of the UV-Vis spectroscopy for the nc-Si(n) layers. The figure shows the absorption coefficients over the wavelength calculated according to equation 36 and the resulting tauc plots according to equation 37 for the determination of the optical band gap. The indicated errors of the band gap result from the errors of the linear fits.

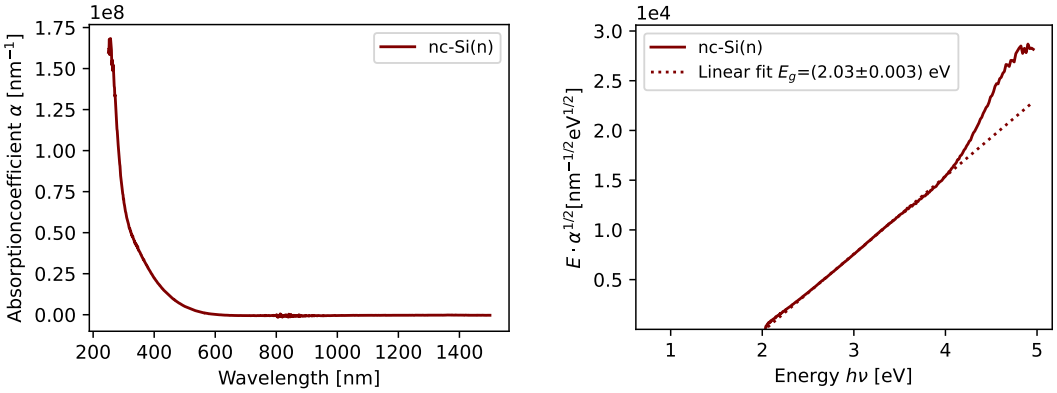

(a) Absorption coefficient **(b)** Tauc plot

Figure 29: Exemplary results of the evaluation of the UV-Vis spectroscopy for the nc-Si(n) single layers on glass substrate. The absorption coefficient (a) and the tauc plot (b) are shown.

The course of the absorption coefficient shows that the coatings absorb little or nothing in the visible and NIR range. Only in the range of wavelengths smaller than approx. 450 nm the absorption increases approximately exponentially. This results in a linear edge in the taucplot, leading to tauc optical band gaps of all the used nc-Si(n) layers within this work of (2.03 ± 0.05) eV. These results are comparable to values on nanocrystalline doped silicon layers from the literature [47, 53], which also exhibit tauc optical band gaps around 2 eV.

5.2.4 Dark Conductivity

Figure 30 shows the Arrhenius plot extracted from the dark conductivity measurement of an example nc-Si(p) singe layer.

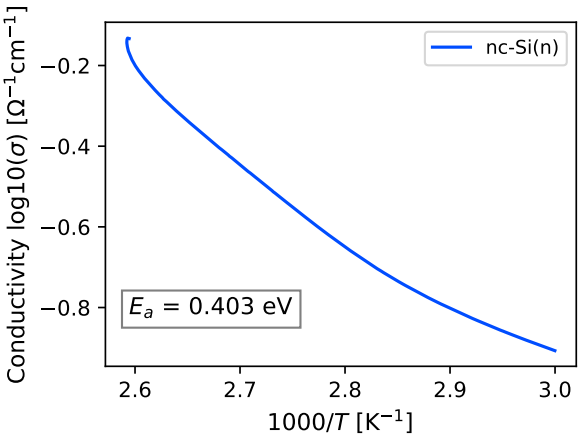

Figure 30: Exemplary Arrhenius plot for an nc-Si(n) layer.

For the exemplary result shown, an activation energy of $E_a = 0.403\,\text{eV}$ can be determined through dark conductivity measurement. This confirms the presence of doping as the middle of the band gap of $E_G = 2.03\,\text{eV}$ would result in an activation energy of approximate 1 eV. On average, the activation energy for the nc-Si(n) layers of all samples is $E_a = (0.38 \pm 0.19)$ eV. This is a relatively large error. However, all samples are clearly n-doped and since there is no correlation of the activation energy of the nc-Si(n) layers with the results later on, this is negligible.

6 Proof-Of-Concept

6.1 Aim of the Experiment

The primary goal of this experiment is to verify whether the cell structure elaborated in the previous chapter is suitable for application as a PEC. The structure concept is to add a p-doped crystalline silicon layer between the Si wafer and the photoanode forming a tunnel recombination junction with the TiO_x photoanode. In this context, it is particularly relevant if the cell performance can be improved by adding the interlayer compared to a cell structure without interlayer. For this work a commercially purchased n-type crystalline Si wafer is used. As the wafer is stored in air, this can lead to the formation of native SiO_2 on the surface. Therefore, an additional question was if a pretreatment of the wafer prior to the interlayer-deposition (to remove native SiO_2 layers) is necessary to produce functional cells at all. The treatment methods used are H_2 passivation and etching with NF_3.

6.2 Experimental Setup

To investigate the previously stated goals of the experiments, six different sample stacks are examined within this experiment, which can be seen in figure 31 along with their sample names. The naming pattern is made according to the following scheme: First, the presence of the interlayer (il) is indicated by a 1, its absence by a 0. In addition, a distinction is made between wafer treatments (tr), whether no treatment (no), H_2-passivation (pa) or NF_3-etching (et) was carried out. Thus, the sample name tr-1_tr-pa indicates that the sample has an interlayer and the wafer has been passivated directly before the deposition of the interlayer.

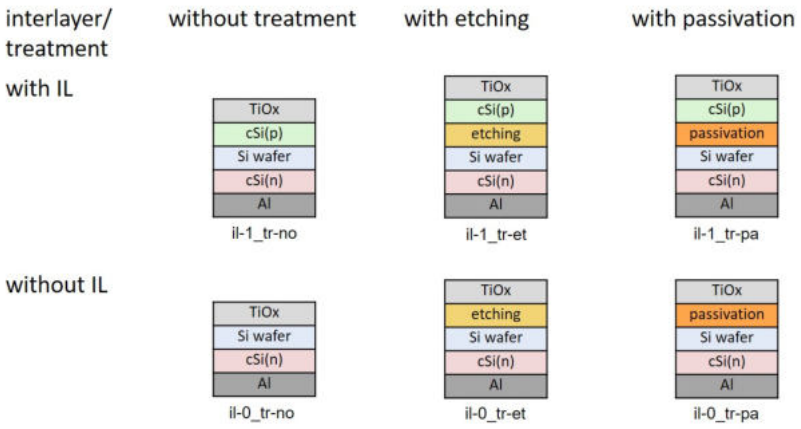

Figure 31: Schematic representation of the sample setup for the first experiment.

For the PECs with p-doped nc-Si, a distinction is made with respect to the wafer

treatment between the samples without treatment, with etching and with passivation. The same pattern results again for the samples without interlayer.

The process parameters for the interlayer deposition can be found in table 3.

Table 3: Parameters for the PECVD process during nc-Si(p) deposition

Parameter	**nc-Si(p)-deposition**
t_{Process} [s]	80
$F_{\mathrm{SiH_4}}$ [sccm]	0.7
$\frac{F_{\mathrm{B_2H_6}}}{F_{\mathrm{SiH_4}}}$ [-]	0.14
$F_{\mathrm{H_2}}$ [sccm]	1000
$\frac{F_{\mathrm{H_2}}}{F_{\mathrm{SiH_4}}}$	200

6.3 Results and Discussion

The following section contains the results and discussion of the characterizations of the individually deposited layers that make up the PEC samples. Since the wafer is commercially available, the backside with the nc-Si(n) layer has already been investigated in chapter 5.2 and the parameters for the TiO_x photoanode have been taken from Berends et al. [7], the single layer characterisation will focus on the interlayer. In addition, the characterisation of the total PEC is carried out. Within the single layer characterization methods, Raman measurements and profilometry results are first evaluated to control the material composition and the layer thickness respectively. Then, mainly for the determination of the optical band gap, the UV-Vis spectrometry data are analyzed. Then the dark conductivity results are used to determine the activation energy. Once the optoelectronic properties of the individual layers are known, the results of the electrochemical characterization of the PECs investigated in this experiment are discussed.

6.3.1 Raman Deconvolution

In figure 32 the results of the deconvolution of the Raman spectra for the c-Si(p) single layers on glass substrate can be seen.

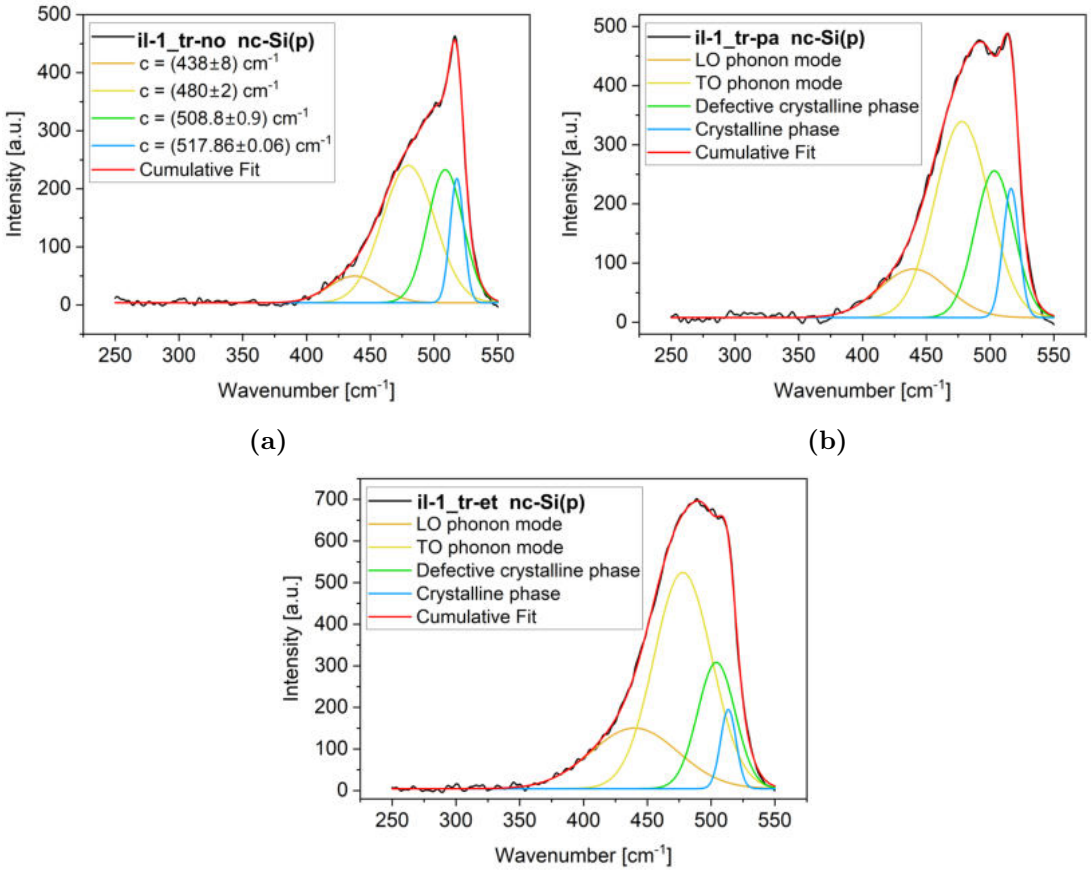

Figure 32: Raman signal deconvolution of nc-Si(p) layers for the samples without wafer treatment (a), with passivation (b) and etching (c). The measured data is given in black. The deconvolution is shown as a cumulative fit (red curve) of the longitudinal optical phonon mode (orange), transversal optical mode (yellow), defective crystalline phase (green) and the crystalline phase (blue) together with the corresponding peak fit centers.

Looking initially only at the measured Raman data, a peak of the crystalline phase between 513 and 517 cm^{-1} can be seen for the single layers of il-1_tr-no and il-1_tr-pa. It is characterized by a sharp peak with adjacent broad shoulder of the peaks of the amorphous phase. For the single layer of il-1_tr-et, the amorphous and crystalline phase peaks are initially indistinguishable in the measured data. Looking at the deconvoluted peaks, however, it becomes clear for all samples that they consist partly of an amorphous phase (orange and yellow curve) and partly of a crystalline phase (green and blue curve).

The results of the determination of the crystallinity factors can be found in table 4. The error information is based on an error propagation calculation of the error of the area information of the individual fits given by the fit with OriginLab.

Table 4: Crystallinity factors of the nc-Si(p) layers.

PEC sample name	p-doped
il-1_tr-no	0.48 ± 0.07
il-1_tr-pa	0.4 ± 0.1
il-1_tr-et	0.30 ± 0.04

The values for the crystallinity factors are between 0.30 and 0.48. Similar values for doped nc-Si layers can also be found in literature [47, 53, 54].

It is striking that the shoulders, caused by the peaks of amorphous origin, become larger from the samples without wafer treatment via passivation to etching. It therefore stands to reason that there could have been an influence of the wafer treatment on the growth of the layers. However, the differences could also be due to the order of the depositions in the chamber. A more detailed investigation could be recommended here for further experiments, especially if there are different results in further measurements.

According to Veprek et al. (1987), with decreasing crystallite size from approx. 10 nm to 3 nm, the peak at $520\,\mathrm{cm}^{-1}$ characteristic of crystalline silicon shifts to lower frequencies up to ca. $512\,\mathrm{cm}^{-1}$ [43]. These data show with decreasing peak from ca. $518\,\mathrm{cm}^{-1}$ toward $513\,\mathrm{cm}^{-1}$ also decreasing crystallity factors. This decrease in crystallity factors could therefore be related to decreasing crystal sizes. However, the results allow the conclusion that the deposited nc-Si(p) layers are nanocrystalline silicon (nc-Si). Therefore, the interlayer will be referred to as nc-Si(p) in the further course of this work.

Figure 33 shows exemplary the measured Raman spectrum of the TiO_x layer on the witness glass from the TiO_x deposition for sample il-0_tr-e.

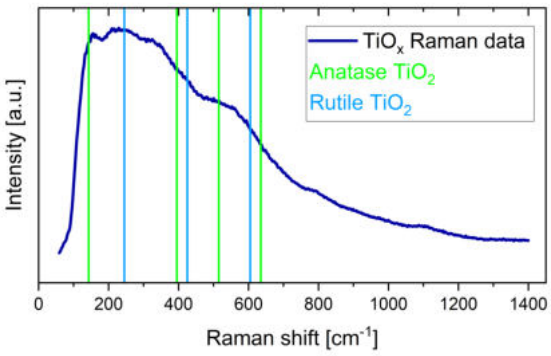

Figure 33: Raman spectrum of the TiO_x layer of the sample il-0_tr-e. Reference Raman peak positions for anatase and rutile TiO_2 are shown and taken from [55]

No clearly sharp peak can be identified. Rather, a broader peak around approx. $250\,cm^{-1}$ can be seen, which has a broad shoulder in the region around $500\,cm^{-1}$. This agrees well with the descriptions of Berends et al. [7]. It can therefore be assumed that the photoanode material deposited in this experiment is the TiO_x described by Berends et al.

6.3.2 Layer Thickness

Table 5 shows the measured thicknesses of the nc-Si(p) single layers on a glass substrate.

Table 5: Measured thicknesses of the nc-Si(p) layers

PEC sample name	**Thickness [nm]**
il-1_tr-no	27 ± 4
il-1_tr-pa	30 ± 3
il-1_tr-et	31 ± 4

The layer thicknesses with the standard deviation correspond to the expected target layer thickness of approx. 30 nm, which is also used as layer thickness in the following calculations.

6.3.3 Tauc Optical Band Gap

The individual layers of the PECs (p- and n-doped nc-Si layers as well as TiO_x layers) on glass substrate and a substrate glass were optically measured in the UV-Vis Spectrometer.

The results of the UV-Vis spectroscopy of the PECVD deposited doped nc-Si(p) can be found in figure 34. The figure shows in a) the absorption coefficients over the wavelength calculated by equation 36 and in b) the resulting tauc plots for the determination of the optical band gap by equation 37. The indicated errors result from the errors of the applied linear fits.

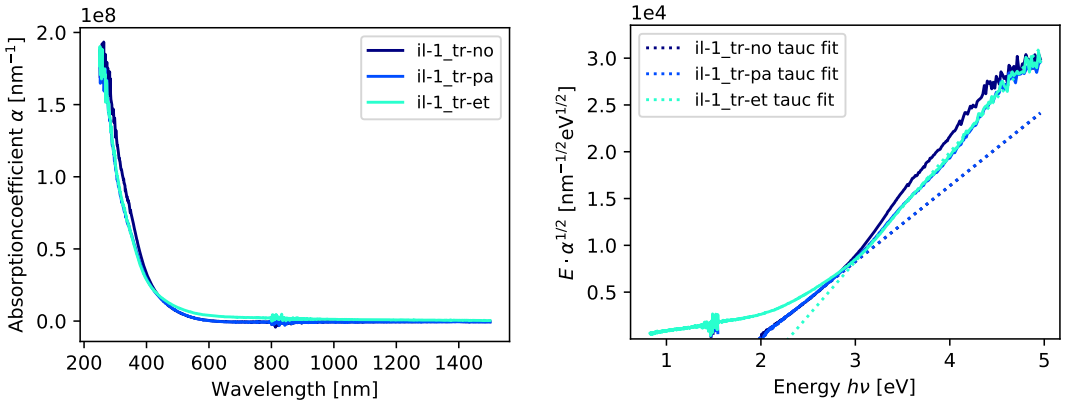

(a) **(b)**

Figure 34: Absorption coefficients and tauc plots for all three nc-Si(p) layers of the experiment. The fits in the tauc plot are shown as dotted lines.

Table 6 shows the determined band gap from the tauc optical band gap fits to the data in the tauc plots.

Table 6: Tauc optical band gaps resulting from the linear fit to the tauc plots.

PEC sample name	Tauc optical band gap [eV]
il-1_tr-no	1.981 ± 0.005
il-1_tr-pa	1.978 ± 0.003
il-1_tr-et	2.289 ± 0.007

The absorption coefficient plot indicates that the nc-Si(p) single layers on glass substrate absorb little or nothing, especially in the visible and NIR range. Only in the range of wavelengths smaller than approx. 450 nm the absorption increases sharply linear. This results in an equally sharp and clear linear edge in the taucplot, leading to tauc optical band gaps from (1.981± 0.005) eV for the nc-Si(p) layer without prior wafer treatment up to (2.289± 0.007) eV. These results are comparable to values from the literature [47, 53], which also show tauc optical band gaps around 2 eV for nc-Si(p) single layers.

6.3.4 Dark Conductivity

As the layer thickness of the individual nc-Si(p) layers is too small to measure the doping concentration directly via Hall measuremtn, the activation energy is determined by measuring the dark conductivity according to subsection 3.2.2. The results of the dark conductivity measurements for the individual nc-Si(p) layers on witness glasses can be seen in figure 35.

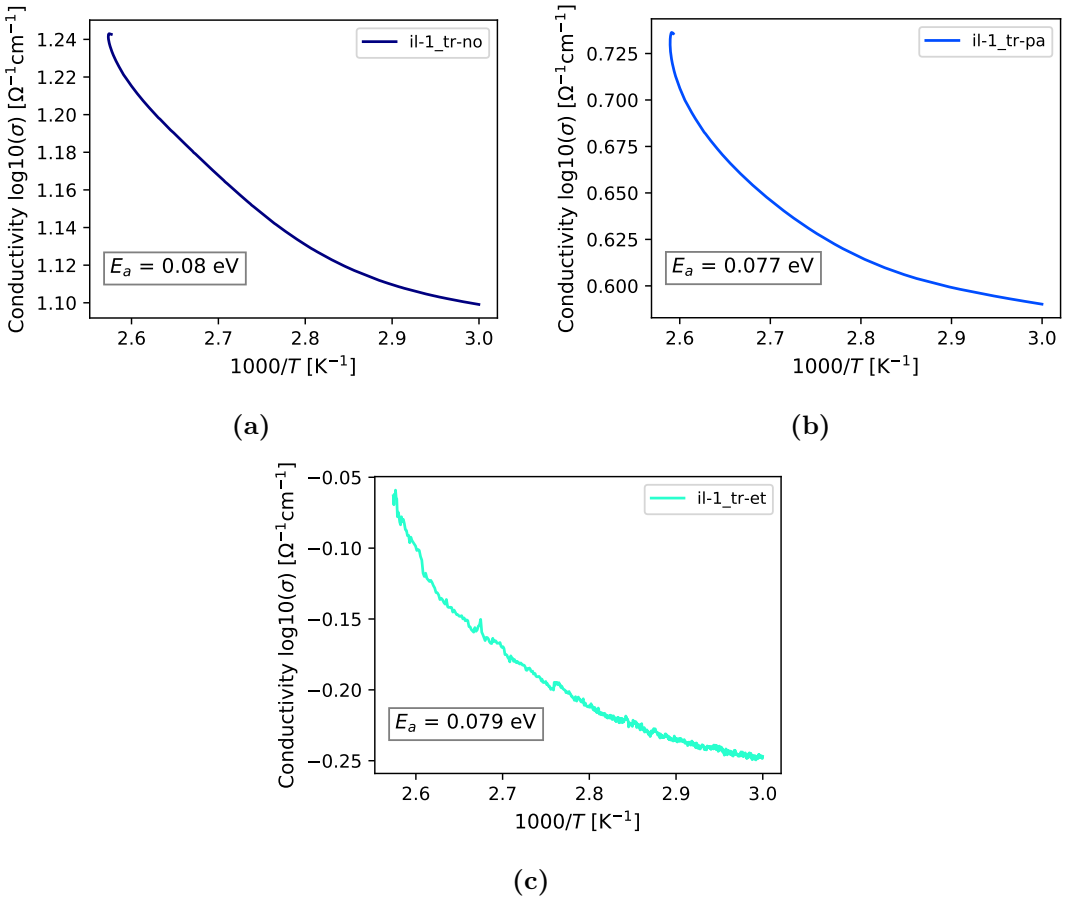

Figure 35: Arrhenius plots as the results of dark conductivity measurements for the nc-Si(p) single layers. The different plots show the conductivity for the nc-Si(p) single layers of the samples a) il-1_tr-no, b) il-1_tr-pa, and c) il-1_tr-et.

The linear fit yields very similar values for the activation energies for all three layers between $E_a = 0.077\,\text{eV}$ for the layer with prior H_2 passivation and $E_a = 0.08\,\text{eV}$ for the layer without prior treatment. The activation energy for the layer with etching is determined to $E_a = 0.079\,\text{eV}$. This means that the distance of the Fermi level to the VBM for the p-doped nc-Si layers is still below 0.1 eV, which is an elaborated value for a suitable activation energy from the simulations with Aforshet (see section 4.3). The requirement of high doping to realize a TRJ at the interface with the n-type photoanode

thus seems to have been achieved.

6.3.5 Electrochemical Characterization

Electrochemical characterization is measured in the form of linear sweep voltammetry measurements on the complete PECs. Each sample was measured three times in succession under irradiation and three times in the dark, resulting in a total of six result curves. In addition to the general trend, the current density at 0 V vs RHE and 1.23 V vs RHE (which is +0.205 V above the potential vs Ag/Ag/Cl) are compared.

Figure 36 shows the results of the three light and dark measurements for each of the six samples. No dark measurement is available for the il-0_tr-no sample because the sample is broken after the light measurements.

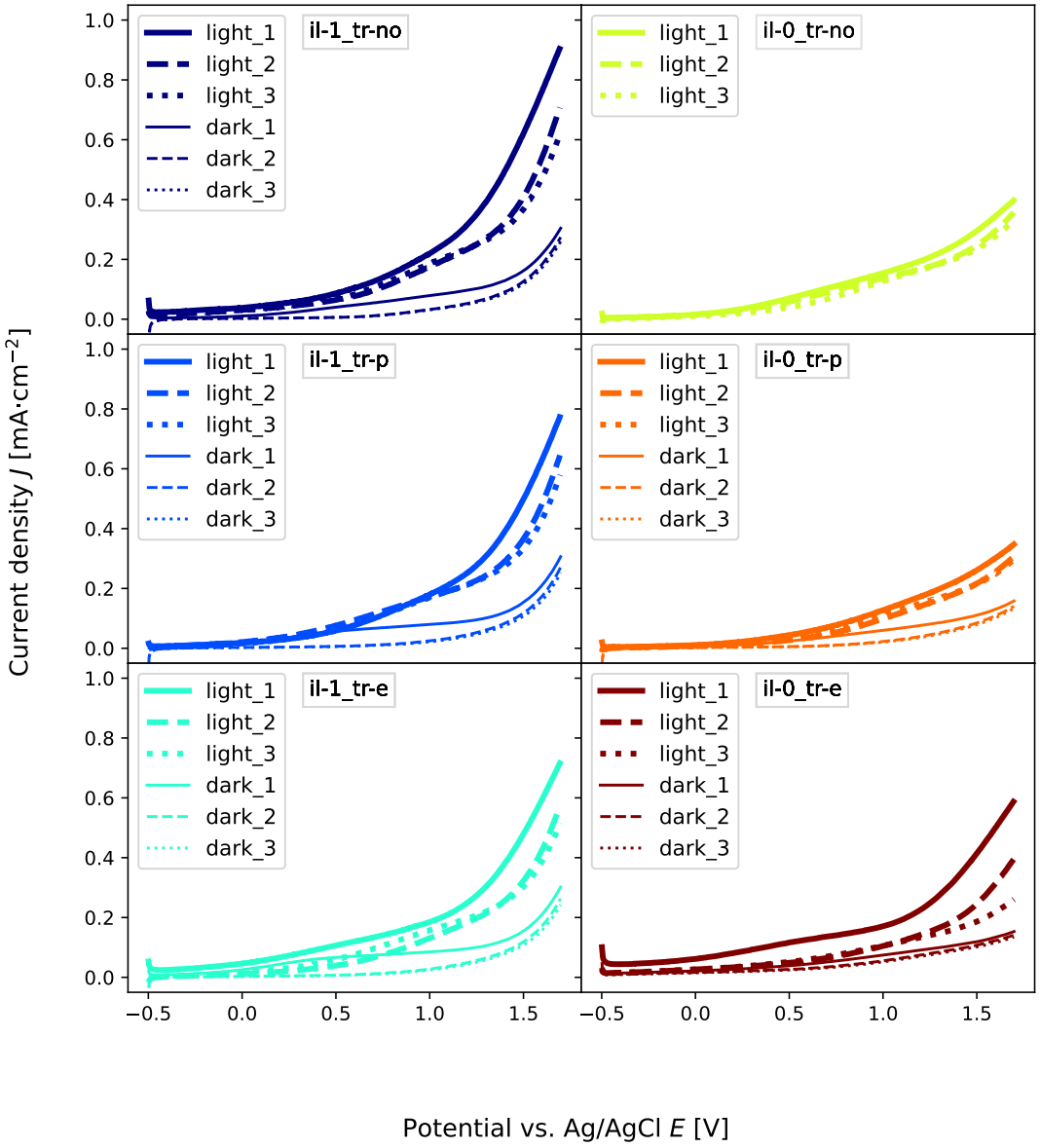

Figure 36: Linear sweep voltammogramms for all samples of the experiment.

Looking first at the general curves, it can be said that the trend of the current densities of all samples for all measurements roughly corresponds to the expected course of the current-voltage curve of a PEC. After there is only a very low current density between -0.5 and 0 V, it starts to increase slightly between 0 and 0.5 V until it shows an almost constant clearly higher slope from about 0.5 to approximately 1.3 V. At approximately 1.3 V, this slope increases again and continues until the end of the measurement at 1.7 V. In addition, a clear difference between illumination and darkness can be seen for all five samples with dark measurements present, demonstrating an increased current density due to photoabsorption. According to Bisquert et al. [13], the materials in

this experiment appear to be stable in the voltage range considered and not corroded, since a current density greater than 0 V is present for the dark measurements.

Furthermore, it is noticeable that with increasing number of measurements a decrease of the current is noticeable. This phenomenon is discussed in more detailin chapter 8.

For a direct comparison between the samples, figure 37 shows the LSV curves of the results of the light measurements of all samples, separated by the measurement number. Figure 40a shows the first, figure 40b the second and figure 37c the third light measurements.

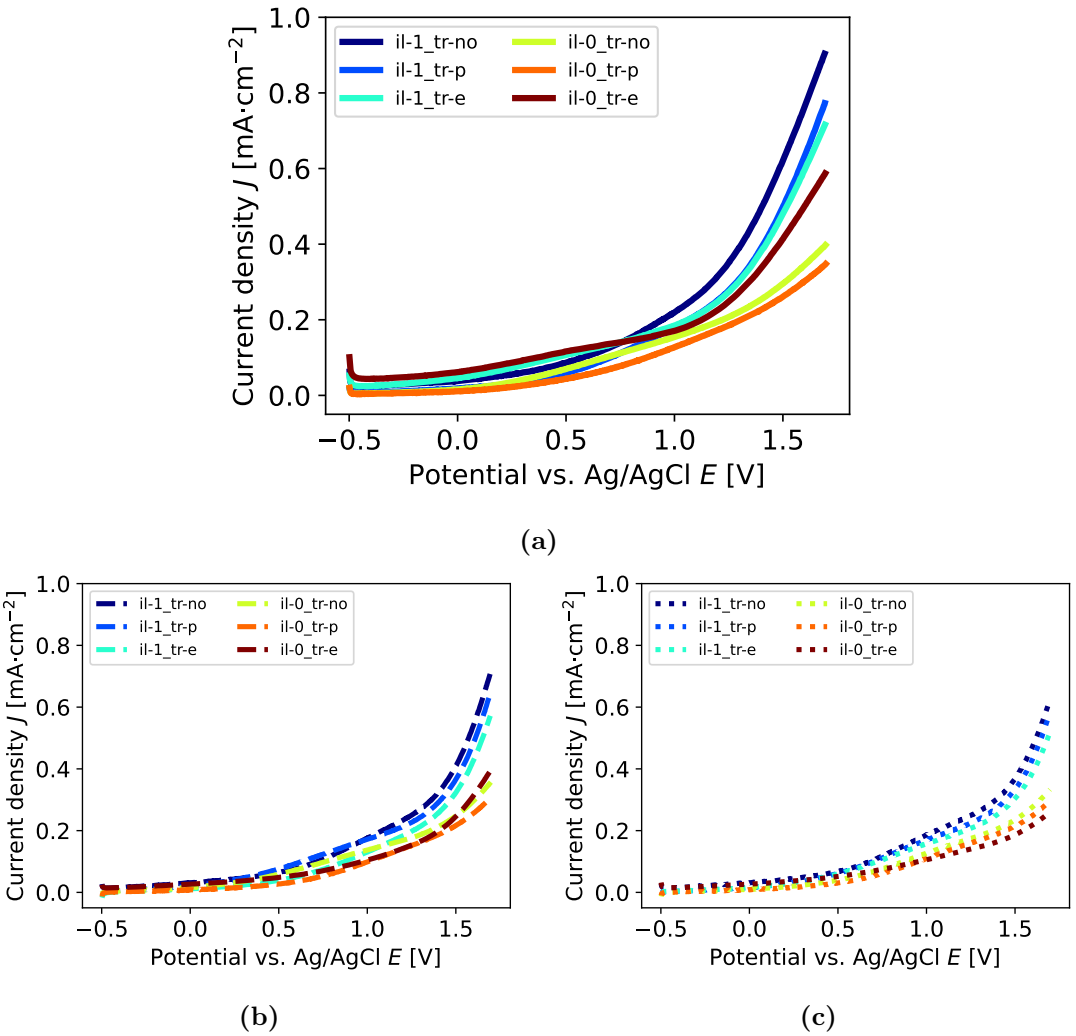

Figure 37: Linear sweep voltammetry plots of the Proof-of-Concept experiment for all samples, plotted for all light measurements seperated according to the measurement number. The first measurements are shown in a), second measurements in b) and the third measurements in c).

The individual values of current density at 0 V and 1.23 V vs RHE and the maximum

values at 1.905 V vs RHE are given in table 7.

Table 7: Current densities at 0 V and 1.23 V vs RHE and the maximum current densities at 1.7 V vs Ag/AgCl.

PEC sample name	J**(0 V vs RHE)** [**mA cm**$^{-1}$]	J**(1.23 V vs RHE)** [**mA cm**$^{-1}$]	$J_{\mathbf{max}}$ [**mA cm**$^{-1}$]
il-1_tr-no	0.052	0.538	0.904
il-1_tr-p	0.029	0.424	0.773
il-1_tr-e	0.067	0.412	0.716
il-0_tr-no	0.03	0.267	0.398
il-0_tr-p	0.02	0.238	0.348
il-0_tr-e	0.082	0.363	0.587

Looking more closely at the results for the first measurements in figure 40a and in table 7, it is noticeable that there are differences between the individual samples. At 0 V vs RHE the PECs for the first measurements reach current densities in the range of approx. 0.02 to 0.08 mAcm^{-2}, which approaches the 0.085 mAcm^{-2} reported by Segev et al. It is noticeable that there seems to be a sorting according to the wafer treatment method. The samples with H_2 passivation have the lowest currents with 0.02 mAcm^{-2} and 0.029 mAcm^{-2} for the sample without and with interlayer respectively. With a current of 0.03 mAcm^{-2} and 0.052 mAcm^{-2}, the two samples without wafer treatment again follow in the order without and with interlayer. The largest current at 0 V vs RHE, 0.067 mAcm^{-2} and 0.082 mAcm^{-2}, is exhibited by the two samples where the wafer was previously etched. Here, however, the sample without interlayer exhibits the higher current. The wafer treatment (etching/passivation) takes place on the Si wafer before the nc-Si(p) layer is deposited and is therefore outside the TRJ. It can therefore be assumed that the influence of the wafer treatment is so small that it only becomes apparent at lower applied voltages. With increasing applied voltages, the external field leads to increasing band bending in the whole cell structure due to an increasing electrostatic potential gradient. In figure 40c it can be seen that the band bending within the Si wafer is not abrupt, but has a relatively low curvature and thus protrudes relatively deep into the wafer. If smaller barriers are encountered here due to native SiO_2, it could be that these can be overcome more easily with larger electrical potential gradients. This could result in the influence of the wafer treatment becoming less apparent at higher applied voltages. Thus, wafer treatment appears to have an effect on cell performance for unassisted water splitting, with NF_3-etching appearing

to improve performance and H_2-passivation appearing to worsen performance relative to untreated wafers.

In the figure, the identifiable differences between the samples are mainly visible in the range > 1 V vs Ag/AgCl. The three samples with nc-Si(p) interlayers (dark blue, blue and turquoise) with similar values and similar slope are particularly striking. Their maximum current densities at 1.7 eV are $0.716\,\mathrm{mAcm^{-2}}$, $0.773\,\mathrm{mAcm^{-2}}$, and $0.904\,\mathrm{mAcm^{-2}}$ for the samples with etching, passivation, and no wafer treatment, respectively. They mainly stand out from the current densities of the samples without IL and without treatment and with H_2 passivation with $0.398\,\mathrm{mAcm^{-2}}$ and $0.348\,\mathrm{mAcm^{-2}}$, respectively (yellow and orange). The sample without IL where the wafer was etched before interlayer deposition has a slope somewhere in between and a maximum current density of $0.587\,\mathrm{mAcm^{-2}}$. Comparing the same wafer treatment to each other, one can see for each of the three pairs that the sample with interlayer has a significantly higher current with a factor of up to 2.3 for the two samples without wafer treatment. Thus, insertion of the interlayer results in an increase in current for each wafer treatment method. It can be surmised here that the TRJ has a positive effect on the performance of the PEC.

Recalling the question of whether prior wafer treatment is necessary for the feasibility of PEC sample fabrication, we obtain comparable results for the samples with interlayer for all treatment methods. For unassisted water splitting, NF_3 etching of the wafer seems to be able to increase the current density. For higher applied potentials, however, even the sample without treatment shows the highest current. For the samples without interlayer it looks a bit different: The sample with etching treatment has the highest current both for 0 V vs RHE and for the maximum applied voltage. However, it is interesting to look at light measurements two and three. In general, it can be said that there was a decrease in current for all samples when repeating the measurement (see chapter 8 for more details). If we look at the maximum currents again, a clear grouping can be seen: As for the first measurements, the three samples with interlayer achieve the largest currents, keeping the order. For the samples without interlayer, the sample that was etched now also has the lowest current.

For the question of the necessity of wafer treatment for the feasibility of PEC sample fabrication, it can be concluded that for further experiments the pretreatment of the wafer is not absolutely needed. It cannot be ruled out that there are parameter configurations, e.g., by optimizing the etching process, in which better results may be obtained with pretreatment. This can be assumed by the larger currents for unassisted water splitting from the etched wafers. However, this is beyond the scope of this work, but is to be investigated for further optimization.

7 Comparison with a TiO2 Photoanode

This chapter describes the experiment comparing the newly developed TiO_x photoanode with the conventional TiO_2 photoanode when integrated into a tandem PEC.

7.1 Aim of the Experiment

As Berends et al. [7] showed, the TiO_x photoanode they developed exhibits increased absorption compared to conventional TiO_2. However, since this only refers to the individual layers, this experiment will verify to what extent the TiO_x photoanode in the tandem PEC structure used in the proof-of-concept also differs from the conventional TiO_2 photoanode in the overall cell structure. At the same time, we want to understand whether the resulting current density for the tandem PECs is not caused by the Si wafer alone, but is the result of the successful integration of the photoanode into a tandem cell.

7.2 Experimental Setup

The sample stack of this experiment can be seen with all samples used in figure 38. For the first comparison, approximate 250 nm thick TiO_x and TiO_2 layers were each inserted into the tandem PEC. A PEC with a an approximate 30 nm thick protective layer of TiO_2 was fabricated to analyze the influence of the silicon wafer. The aim of the TiO_2 layer is to avoid photocorrosion reactions in aqeous solution under ilumination [27]. In order to distinguish the samples, those with the significantly thicker layers are called absorber layer (AL) and those with the thin layer protection layer (PL). For all samples, the same interlayer of nc-Si(p) as used in the proof-of-concept was added between the wafer and photoanode material. All layers are fabricated as in the proof-of-concept experiment. As a result of the proof-of-concept analysis the wafer was not treated.

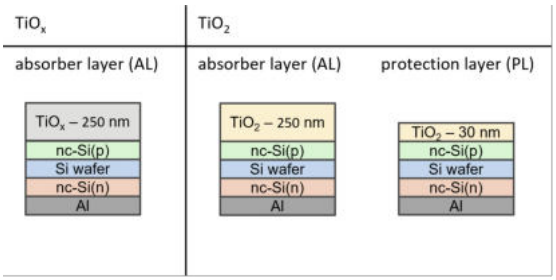

Figure 38: Schematic representation of the sample setup. The material TiO_x is shown in gray, and TiO_2 in yellow.

For this experiment, the Si wafers are broken down to an area of approximately 6 x 6 cm^2 and the smaller 3D print is used for the LSV structure, resulting in an active area of

11.95 cm.

7.3 Results and Discussion

Since only other materials or layer thicknesses of the photoanodes are varied in this experiment, the focus of the single layer characterization is on the photoanode layers. The other layers have been characterized in previous chapters.

7.3.1 Raman Spectroscopy

In figure 39, the results of Raman measurements of the TiO_x and TiO_2 layers on glass substrate are shown. The Raman shift characteristics of anatase and rutile phase are plotted for reference.

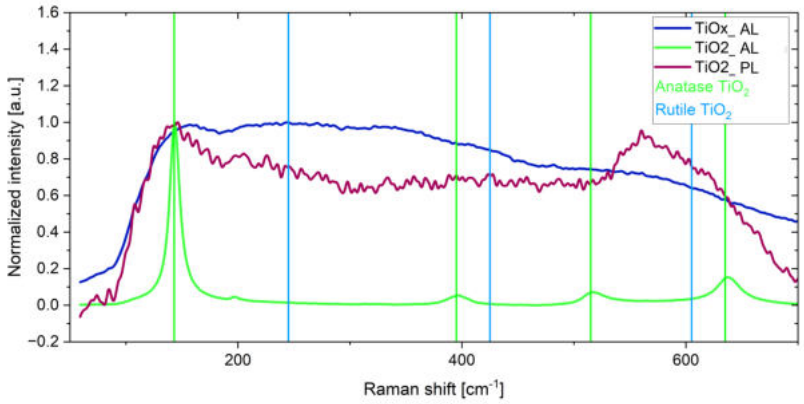

Figure 39: Raman signal of the photoanode layers used in this experiment. The Raman shift characteristics of anatase and rutile phase are plotted for reference.

For the layer of sample TiO_2_AL, a clear distinct peaks can be seen at the Raman shifts characteristic of anatase. The layer of sample TiO_x_AL again shows the broad peak around 250 cm^{-1} with a very broad shoulder around 250 cm^{-1}, as also noted by Berends et al. For the thin film of the TiO_2_PL sample, the signal is less clear. A peak is seen at 143 cm^{-1}, which is considered characteristic of anatase. The peak at 570 cm^{-1} is not related to neither anatase nor rutile phase. Since the cause of Raman shifts lies in the atomic bonds, even small changes in the bonds can lead to altered peaks. It is therefore possible that impurities could have occurred in the very thin layer.

7.3.2 Layer Thickness

Table 8 shows the results of the profilometry measurements for the TiO_x and TiO_2 layers.

Table 8: Measured thicknesses of the TiO_x and TiO_2 layers

PEC sample name	**Thickness [nm]**
TiO_x_AL	291 ± 8
TiO_2_AL	270 ± 10
TiO_2_PL	32 ± 4

Slightly larger film thicknesses than the target film thicknesses were measured in each case. However, the TiO_x_AL and TiO_2_AL layers at (291 ± 8) nm and (270 ± 10) nm are comparable with the targeted thickness of 250 nm. The TiO_2 layer used as a protective layer is (32 ± 4) nm, which is on the order of the target thickness of 30 nm.

7.3.3 Electrochemical Characterization

In figure 40 LSV measurements under illumination and in the dark are shown as linear sweep voltammogram for each sample individually.

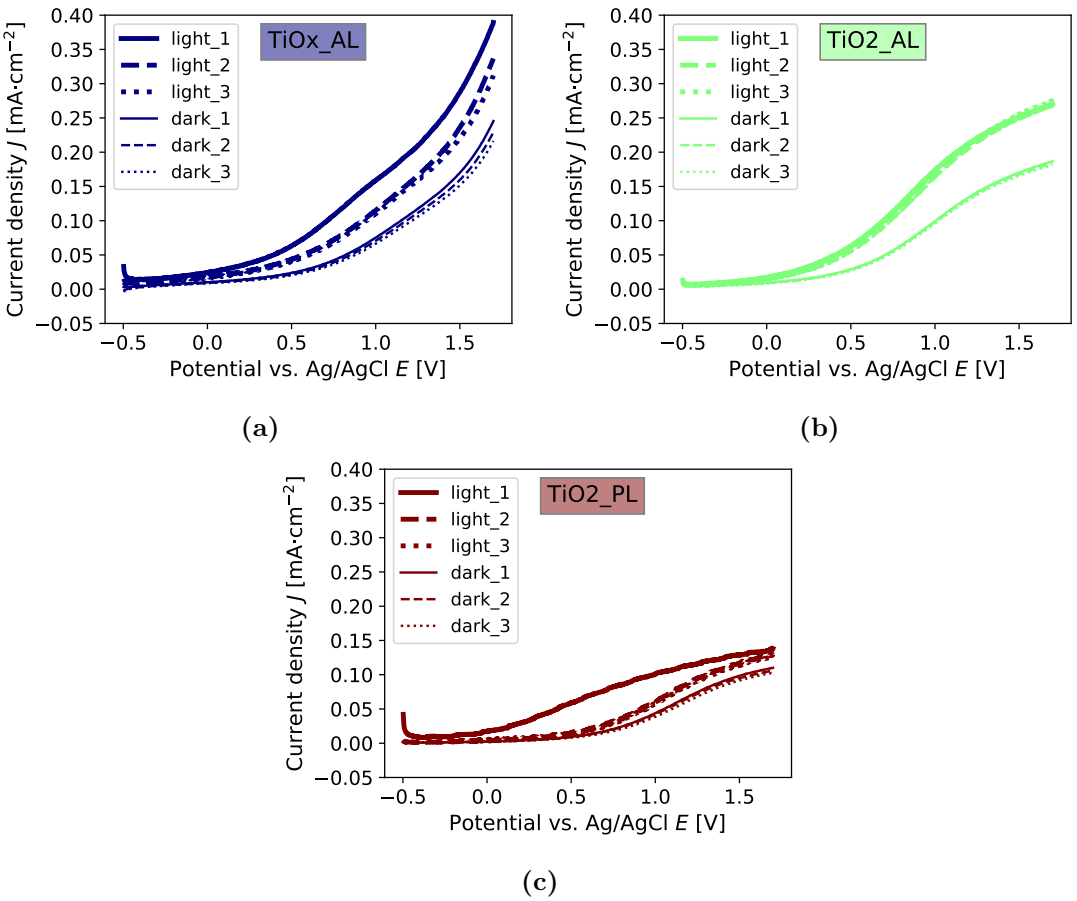

Figure 40: Linear sweep voltammogramms for every sample. Shown are three measurements each, which were performed under irradiation and in the dark.

It can be seen that the materials of the samples are not corroded as they all exhibit dark currents. As expected, the TiO_x sample shows a similar curve to the sample with the same parameters from the proof-of-concept experiment. Only the absolute values of the current density are significantly lower. The maximum current measured at 1.7 V vs RHE is here 0.389 $mAcm^{-2}$. For this experiment, the smaller setup was used. Since the resistance of the electrolyte increases with greater distance [56], it is suspected that the longer distance between the platinum wire and photoelectrode in the smaller setup results in the lower current. However, since a uniform sample setup was used for all samples within one experiment, the results within one experiment are comparable to each other.

For a direct comparison of the samples with each other, the LSV curves of the measurements under irradiation for the three samples are shown in figure 41, separated by their measurement number.

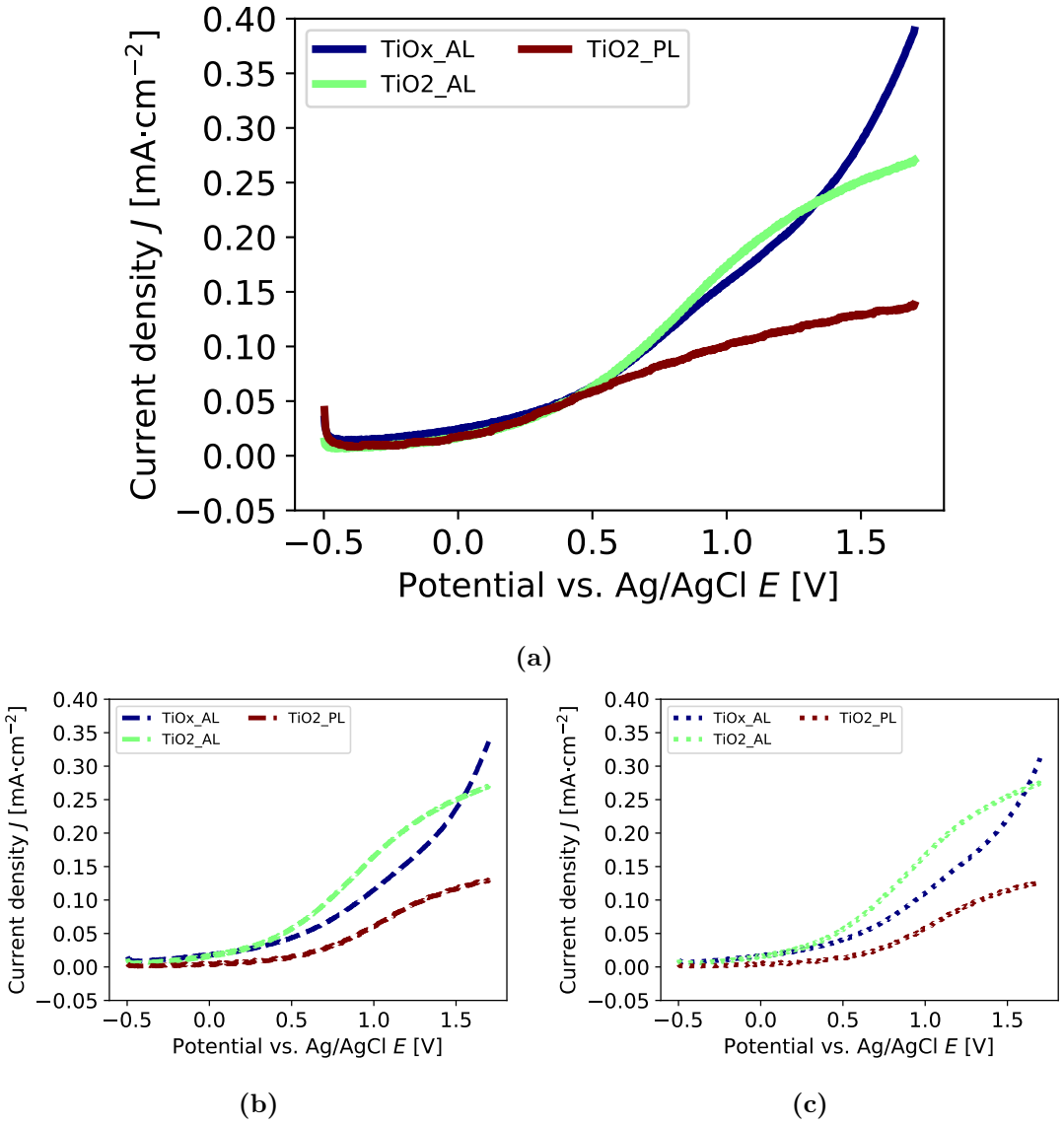

Figure 41: Linear sweep voltammograms for the three samples in this experiment showing the first (a), second (b) and third (c) LSV measurements under irradiation.

If the first measurements are compared with each other, clear differences in the curve become apparent. The curve shapes of the samples TiO_x_AL and TiO_2_AL are similar up to approx. 1.0 V. However, for voltages > 1.0 V the slope for the sample with TiO_2 starts to saturate while the curve for the TiO_x tandem PEC keeps increasing. The current density for the curve of TiO_2 at 1.7 V is then 0.271 mAcm^{-2} compared to the 0.389 mAcm^{-2} for the sample with the TiO_x photoanode. It stands to reason that this increase in current density is due in part to the increased absorption of the TiO_x. In addition, the substoichiometric TiO_x may have created oxygen vacancies where increased OER can take place.

The sample with a thin TiO_2 layer of approx. 30 nm, on the other hand, already shows a significantly lower current density from approx. 0.5 V than both other samples. The slope also starts to decrease and at the end at 1.7 V a current density of 0.138 $mAcm^{-2}$ can be seen. It can be assumed that photoabsorption occurs mainly in the Si wafer due to the very thin TiO_2 layer. As a result, the theoretical minimum voltage of 1.23 V required for water splitting (losses not yet included) would be expected to be reached much later and thus the onset potential would be higher than for the tandem cells. However, this cannot be observed for the first measurement. Nevertheless, it can be seen that the current density increases only more slowly. This slower increase leads to a significantly lower current density even for an applied potential of 1.7 V for the sample with 30 nm TiO_2, which could be due to the lower reactivity toward O_2 in comparison to TiO_x. Figure 41b shows the second LSV measurement under irradiation of each sample. A similar behavior as for the first measurement can be observed for the TiO_2_AL sample. The TiO_x photoanode on the TiO_x_AL sample seems to lead to a reduced the current density for the second measurement compared to the TiO_2 photoanode. The reduced current density can be clearly seen in the region starting at an applied voltage of 0.5 V. This also decreases the difference in current densities at 1.7 V: The sample with TiO_x has a decreased current density of 0.337 $mAcm^{-2}$ and the sample with TiO_2 with 0.271 $mAcm^{-2}$ has not experienced a decrease in current density compared to the first measurement. For the LSV curve of the sample TiO_2_PL, the onset potential increased by approx. 0.6 V. Why this increased onset potential compared to the tandem cells is only observed for the second light measurement cannot be clearly explained. A possible explanation could be that the thin TiO_2 layer lead to reactions with a native SiO_2 layer formed on the surface of the wafer which was not removed by the non-treatment.

The third measurements in each case can be seen in figure 41c. For these, the trend of decrease in current density for the sample with TiO_x continues. This could also be seen in the proof-of-concept and is therefore consistent with the results. The LSV curves of the TiO_2_AL and TiO_2_PL samples appear to show an unchanged current density.

8 Device Degradation

8.1 Aim of the Experiment

In the course of the electrochemical characterisation of the previous experiments, a change in the current density was observed with repetitions of the measurement. Therefore, this experiment will show why the first three measurements were considered in the evaluation.

8.2 Experimental Setup

For the investigation, 20 LSV measurements under irradiation are performed one after the other with a time interval of one minute between each measurement. The measurements are numbered in ascending order from 1. To avoid heat exchange, the door of the climate chamber remains closed for the duration of the entire experiment.

8.3 Results and Discussion

Figure 42 shows the time-dependent behavior of a PEC (same layer stack as il-1_tr-no) for a linear scan voltammetry. Since there is not much change in the trend between measurement 10 and 20, only the first 10 measurements are shown here.

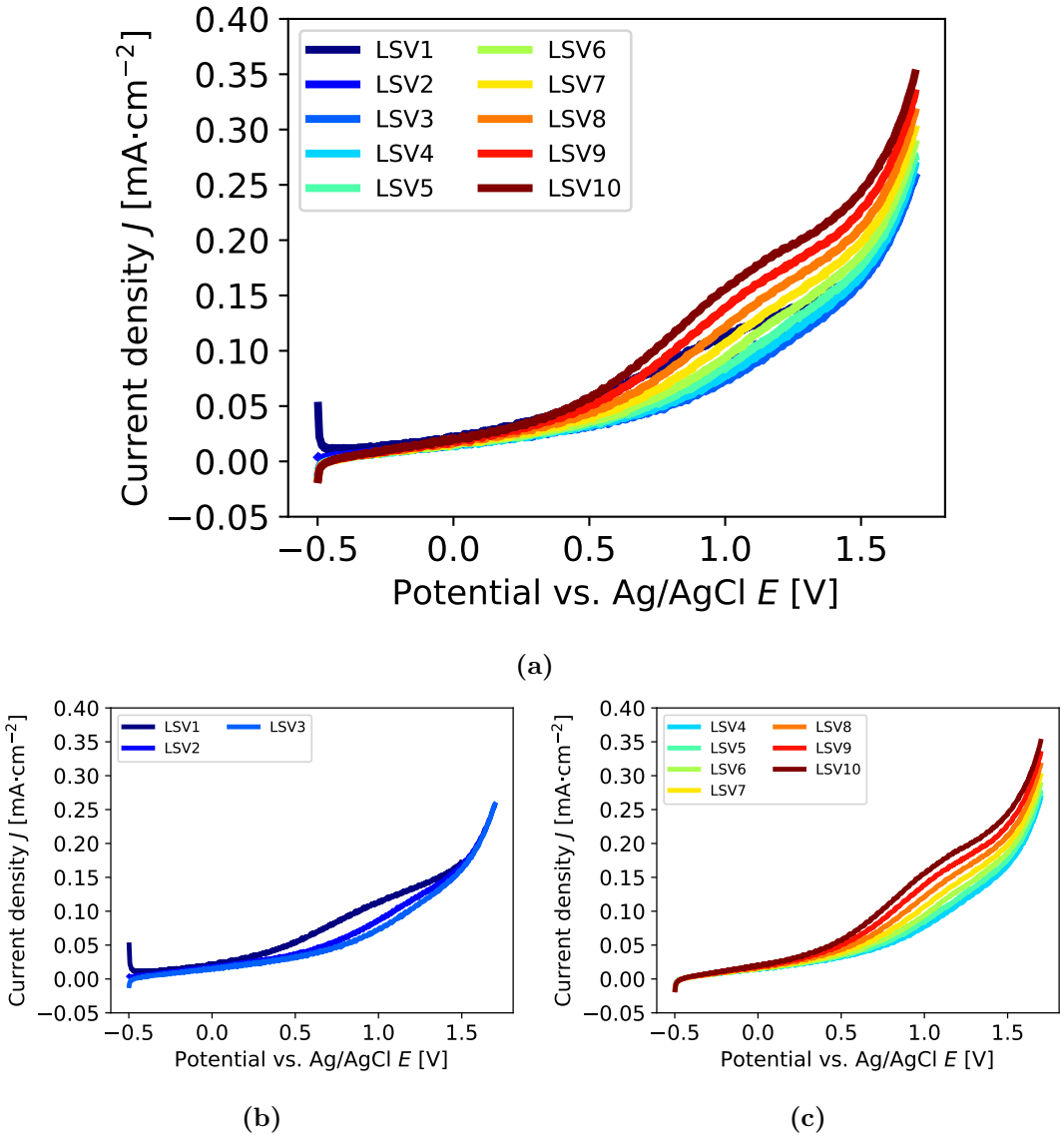

Figure 42: Linear sweep voltammogramms of one PEC device for 10 consecutive light measurements. a) shows all 10 LSV curves in one plot, whereas the first three measurements are shown in b) separated from the following measurements 4-10 in c).

Figure 42a shows the first 10 measurements all in one plot. It can be seen that the curves partially overlap. Therefore, the curves are grouped into two subplots: Figure 42b contains the measurements with a decreasing trend (measurement 1-3). It can be seen, especially in the range of ca. $0.3 - 0.5$ V, there is a significant decrease in the current density from the first to the third measurement. At the same time, the characteristic of the current curve also changes, since the onset of the increase of the current is shifted towards higher potentials. It should be noted that the difference in current density from measurement 1 to 2 is significantly greater than the difference from measurement

2 to 3. A possible explanation for this decrease in current density could be that the oxygen vacancies initially present become more and more saturated in the course of a measurement, so that fewer oxygen vacancies are present for the next measurement.

From measurement 3 onwards, the current density starts to increase, what can be seen in figure 42c. It seems that the currents increase more and more and also the onset potential shifts to lower potentials. Thus, an increasingly lower applied potential is sufficient to lead to an increase in current density. Additionally, a saddle point seems to form.

From approximately 10 min after the measurement start there was a continuous, approximately linear increase in temperature inside the climatic chamber from 25 C to around 35 C toward the end (measurement 20). It stands to reason, especially from the correlation of the increase in the conductivity of semiconductor materials with increasing temperature, that the increase in current density from measurement 3 onward is due to the temperature increase of the climatic chamber and the associated heating of the experimental setup (especially electrolyte and sample).

Due to the trend reversal from measurement 3 onwards, it is assumed that the oxygen vacancies are comparatively saturated from then onwards, so that there is no longer any significant decrease and the influence of the temperature predominates. It is also possible that the chamber or the electrolyte with the semiconductor have heated up after 10 minutes so that this has an influence on the conductivity.

This is the reason why three light measurements are always carried out in succession in this work. For the subsequent dark measurements, the irradiation of the experimental setup is prevented by putting an opaque box over it, which is why the effects of the previous temperature increase should also be small here. Due to the observed influence of the temperature after 10 minutes, the measurement was always started immediately after insertion of the setup into the climate chamber. Nevertheless, variations in the start time cannot be excluded and are attributed to the external error. This is the reason why all three light and dark measurements are shown in each case so that trends can be seen.

9 Summary and Conclusion

The aim of this thesis was to identify a suitable interlayer material for the integration of the newly developed TiO_x Photoanode onto a silicon wafer. The selected material should then be used to verify whether functional tandem PECs can be produced in the present laboratory conditions.

To achieve this, first analysis of the band diagrams for the existing silicon wafer in direct contact with the TiO_x photoanode were performed. It was found that a c-doped material could allow tunneling of electrons from the photoanode into the Si wafer. This results in a tunnel recombination junction between the Photoanode and the p-doped material. As a possible candidate, p-doped nc-Si was identified due to tunable doping possibility and existing expertise in the laboratory.

In a subsequent proof-of-concept experiment, it was possible to demonstrate that nc-Si(p) is suitable as an interlayer material and can significantly increase the current density during an LSV measurement compared to samples without an interlayer. It was shown that the current density is the result of a successful integration of the single materials into a functional tandem PEC. Moreover, it could be confirmed that the off-stochiometric TiO_x layer enables higher current densites compared to conventional TiO_2 layer when integrated into a tandem PEC device. However, a significantly larger decrease in current density was observed for the PECs with a TiO_x photoanode during the first three measurements compared to TiO_2 as photoanode material. It is assumed that these are saturations of oxygen vacancies at the surface of TiO_x, reducing the reactive sites for the OER at the TiO_x surface. For an application as a photoanode in a tandem PEC, this performance decrease should be investigated in more detail and avoided if possible.

Thus, from these results, it can be concluded that nc-Si(p) is suitable as a material for the interlayer and functioning tandem PECs can be fabricated with the laboratory conditions. Further optimization of the tandem PEC stack seems reasonable at this point. A next possible step for following work would be to experimentally verify which layer thickness and which doping concentration of the nc-Si(p) layer optimizes the cell performance. In addition, a hole-blocking layer between photoanode and nc-Si(p) could be added, offering a lower level of VBM than that of the photoanode to reduce recombination at the TRJ. Furthermore, more detailed investigation of the influence of wafer etching could be undertaken to improve the ability for unassisted water splitting.

References

[1] UNFCCC. Paris agreement. `https://unfccc.int/process-and-meetings/the-paris-agreement/the-paris-agreement`, 2015. accessed on 01.02.2023.

[2] Meng-Tian Huang and Pan-Mao Zhai. Achieving paris agreement temperature goals requires carbon neutrality by middle century with far-reaching transitions in the whole society. *Advances in Climate Change Research*, 12(2):281–286, 2021.

[3] Matthew A. Pellow, Christopher J. M. Emmott, Charles J. Barnhart, and Sally M. Benson. Hydrogen or batteries for grid storage? a net energy analysis. *Energy & Environmental Science*, 8(7):1938–1952, 2015.

[4] A. Fujishima and K. Honda. Electrochemical photolysis of water at a semiconductor electrode. *Nature*, (VOL. 238), 1972.

[5] J. Nowotny, T. Bak, M. Nowotny, and L. Sheppard. Titanium dioxide for solar-hydrogen i. functional properties. *International Journal of Hydrogen Energy*, 32(14):2609–2629, 2007.

[6] Shaohua Shen, Jie Chen, Meng Wang, Xia Sheng, Xiangyan Chen, Xinjian Feng, and Samuel S. Mao. Titanium dioxide nanostructures for photoelectrochemical applications. *Progress in Materials Science*, 98:299–385, 2018.

[7] Dennis Berends, Patrick Schwager, Kai Gehrke, Martin Vehse, and Carsten Agert. Effect of asymmetric power distribution in bipolar reactive sputtering on the optoelectronic and microstructure properties of titanium dioxide for solar water splitting. *Vacuum*, 203:111290, 2022.

[8] Gideon Segev, Jeffrey W. Beeman, Jeffery B. Greenblatt, and Ian D. Sharp. Hybrid photoelectrochemical and photovoltaic cells for simultaneous production of chemical fuels and electrical power. *Nature materials*, 17(12):1115–1121, 2018.

[9] Weicong Li and Harry Kwok. Conduction mechanisms in organic semiconductors. pages 493–500, 2012.

[10] Chunfu Zhang, Jincheng Zhang, Xiaohua Ma, and Qian Feng. *Semiconductor Photovoltaic Cells*. Springer Singapore, Singapore, 2021.

[11] Wolfgang Demtröder. Experimentalphysik 3. *Springer Berlin Heidelberg*, 2016.

[12] Peter Würfel. Physics of solar cells: From principles to new concepts. *Wiley-VCH*, 2005.

[13] Juan Bisquert and Sixto Giménez, editors. *Photoelectrochemical Solar Fuel Production: From Basic Principles to Advanced Devices*. Springer International Publishing and Imprint: Springer, Cham, 1st ed. 2016 edition, 2016.

[14] A. Rockett. *The materials science of semiconductors*. Springer, New York, 2008.

[15] David J. Griffiths. *Introduction to Quantum Mechanics*. Prentice Hall, 1995.

[16] Xiao LI. High-efficiency si solar cell including tunnel junction for tandem photovoltaic cells. 2021.

[17] N. Moulin, M. Amara, F. Mandorlo, and M. Lemiti. Tunnel junction i (v) characteristics: Review and a new model for p-n homojunctions. *Journal of Applied Physics*, 126(3):033105, 2019.

[18] Qi Chen, Guozheng Fan, Hongwei Fu, Zhaosheng Li, and Zhigang Zou. Tandem photoelectrochemical cells for solar water splitting. *Advances in Physics: X*, 3(1):1487267, 2018.

[19] Michele de Bastiani, Anand S. Subbiah, Erkan Aydin, Furkan H. Isikgor, Thomas G. Allen, and Stefaan de Wolf. Recombination junctions for efficient monolithic perovskite-based tandem solar cells: physical principles, properties, processing and prospects. *Materials Horizons*, 7(11):2791–2809, 2020.

[20] Leo Esaki. New phenomenon in narrow germanium p-n junctions. *Phys. Rev*, 109:603, 1958.

[21] Jonathan P. Mailoa, Colin D. Bailie, Eric C. Johlin, Eric T. Hoke, Austin J. Akey, William H. Nguyen, Michael D. McGehee, and Tonio Buonassisi. A 2-terminal perovskite/silicon multijunction solar cell enabled by a silicon tunnel junction. *Applied Physics Letters*, 106(12):121105, 2015.

[22] Alain Rolland, Laurent Pedesseau, Mickaël Kepenekian, Claudine Katan, Yong Huang, Shijian Wang, Charles Cornet, Olivier Durand, and Jacky Even. Computational analysis of hybrid perovskite on silicon 2-t tandem solar cells based on a si tunnel junction. *Optical and Quantum Electronics*, 50(1), 2018.

[23] Heping Shen, Stefan T. Omelchenko, Daniel A. Jacobs, Sisir Yalamanchili, Yimao Wan, Di Yan, Pheng Phang, The Duong, Yiliang Wu, Yanting Yin, Christian Samundsett, Jun Peng, Nani Wu, Thomas P. White, Gunter G. Andersson, Nathan S. Lewis, and Kylie R. Catchpole. In situ recombination junction between p-si and tio2 enables high-efficiency monolithic perovskite/si tandem cells. *Sci. Adv.*, 4(eaau9711), 2018.

[24] Marko Jošt, Tobias Bertram, Dibyashree Koushik, Jose A. Marquez, Marcel A. Verheijen, Marc D. Heinemann, Eike Köhnen, Amran Al-Ashouri, Steffen Braunger, Felix Lang, Bernd Rech, Thomas Unold, Mariadriana Creatore, Iver Lauermann, Christian A. Kaufmann, Rutger Schlatmann, and Steve Albrecht. 21.6%-efficient monolithic perovskite/cu(in,ga)se 2 tandem solar cells with thin conformal hole transport layers for integration on rough bottom cell surfaces. *ACS Energy Letters*, 4(2):583–590, 2019.

[25] H. Reiss. The fermi level and the redox potential. *The Journal of Physical Chemistry*, 89(18):3783–3791, 1985.

[26] Praveen Kumar and Pooja Devi, editors. *Photoelectrochemical Hydrogen Generation: Theory, Materials Advances, and Challenges*. Springer eBook Collection. Springer Singapore and Imprint Springer, Singapore, 1st ed. 2022 edition, 2022.

[27] Chaoran Jiang, Savio J. A. Moniz, Aiqin Wang, Tao Zhang, and Junwang Tang. Photoelectrochemical devices for solar water splitting - materials and challenges. *Chemical Society reviews*, 46(15):4645–4660, 2017.

[28] J. Nowotny, T. Bak, M. K. Nowotny, and L. R. Sheppard. Tio2 surface active sites for water splitting. *The journal of physical chemistry. B*, 110(37):18492–18495, 2006.

[29] W. R. Fahrner. *Amorphous siliconCrystalline silicon heterojunction solar cells*. SpringerBriefs in applied sciences and technology. Springer, Heidelberg and New York, 2013.

[30] H. Kang. Crystalline silicon vs. amorphous silicon: the significance of structural differences in photovoltaic applications. *IOP Conference Series: Earth and Environmental Science*, 726(1):012001, 2021.

[31] M. Morita, T. Ohmi, E. Hasegawa, M. Kawakami, and M. Ohwada. Growth of native oxide on a silicon surface.

[32] H. Nishino, N. Hayasaka, and H. Okano. Damage–free selective etching of si native oxides using nh 3 /nf 3 and sf 6 /h 2 o down–flow etching. *Journal of Applied Physics*, 74(2):1345–1348, 1993.

[33] V. Atluri, N. Herbots, D. Dagel, S. Bhagvat, and S. Whaley. Hydrogen passivation of si(100) wafers as templates for low temperature (t<100°c) epitaxy. *Nuclear Instruments and Methods in Physics Research*, 1996.

[34] J. Nowotny, T. Bak, M. Nowotny, and L. Sheppard. Titanium dioxide for solar-hydrogen ii. defect chemistry. *International Journal of Hydrogen Energy*, 32(14):2630–2643, 2007.

[35] Milton Ohring. Chemical vapor deposition. In *Materials Science of Thin Films*, pages 277–355. Elsevier, 2002.

[36] Neelesh Jain, Mayur Sawant, Sagar Nikam, and Suyog Jhavar. *Metal Deposition: Plasma-Based Processes*, page 19. 01 2016.

[37] Eugen Unger. Die erzeugung dünner schichten: Das pecvd-verfahren: Gasphasenabscheidung in einem plasma. *Chemie in unserer Zeit*, 25. Jahrg.(Nr. 3), 1991.

[38] Arvind Shah. *Thin-film silicon solar cells*. EPFL Press, Lausanne, 1. edition edition, 2010.

[39] S. M. Rossnagel. Thin film deposition with physical vapor deposition and related technologies. *Journal of Vacuum Science & Technology A: Vacuum, Surfaces, and Films*, 21(5):S74–S87, 2003.

[40] Leonard R. Enlow and James J. Licari. *Hybrid microcircuit technology handbook: materials, processes, design, testing and production: Thin Film Processes*. William Andrew, 1998.

[41] Coralie Charpentier. Investigation of deposition conditions and annealing treatments on sputtered zno:al thin films: Material properties and application to microcristalline silicon solar cells. 12 2012.

[42] R. Raciti, R. Bahariqushchi, C. Summonte, A. Aydinli, A. Terrasi, and S. Mirabella. Optical bandgap of semiconductor nanostructures: Methods for experimental data analysis. *Journal of Applied Physics*, 121(23):234304, 2017.

[43] S. Veprek, F. -A. Sarott, and and Z. Iqbal. Effect of grain boundaries on the raman spectra, optical absorption, and elastic light scattering in nanometer-sized crystalline silicon.

[44] Patrycja Makuła, Michał Pacia, and Wojciech Macyk. How to correctly determine the band gap energy of modified semiconductor photocatalysts based on uv-vis spectra. *The journal of physical chemistry letters*, 9(23):6814–6817, 2018.

[45] University of Warwick. Hall effect measurement. `https://warwick.ac.uk/fac/sci/physics/current/postgraduate/regs/mpagswarwick/ex5/techniques/electronic/hall-effect/`, 27.01.2023. accessed on 27.01.2023.

[46] Inamuddin, Rajender Boddula, and Abdullah M. Asiri. *Self-standing Substrates: Materials and Applications*.

[47] E. Fathi, Y. Vygranenko, M. Vieira, and A. Sazonov. Boron-doped nanocrystalline silicon thin films for solar cells. *Applied Surface Science*, 257(21):8901–8905, 2011.

[48] OriginLab Corporation. Origin, version origin2022b.

[49] T. Berger, D. Monllor-Satoca, M. Jankulovska, T. Lana-Villarreal, and R. Gómez. The electrochemistry of nanostructured titanium dioxide electrodes. *ChemPhysChem*, 13:2824–2875, 2012.

[50] Takashi Hisatomi, Jun Kubota, and Kazunari Domen. Recent advances in semiconductors for photocatalytic and photoelectrochemical water splitting. *Chemical Society reviews*, 43(22):7520–7535, 2014.

[51] R. Varache, C. Leendertz, M. E. Gueunier-Farret, J. Haschke, D. Muñoz, and L. Korte. Investigation of selective junctions using a newly developed tunnel current model for solar cell applications. *Solar Energy Materials and Solar Cells*, 141:14–23, 2015.

[52] Yajie Wang, Robert Wenisch, Rutger Schlatmann, and Iver Lauermann. Inorganic materials as hole selective contacts and intermediate tunnel junction layer for monolithic perovskite–cigse tandem solar cells. *Advanced Energy Materials*, 2018.

[53] Chao Song, Jun Xu, Guran Chen, Hongcheng Sun, Yu Liu, Wei Li, Ling Xu, Zhongyuan Ma, and Kunji Chen. High-conductive nanocrystalline silicon with phosphorous and boron doping. *Applied Surface Science*, 257(4):1337–1341, 2010.

[54] X. Jia, Z. Lin, T. Zhang, B. Puthen-Veettil, T. Yang, K. Nomoto, J. Ding, G. Conibeer, and I. Perez-Wurfl. Accurate analysis of the size distribution and crystallinity of boron doped si nanocrystals via raman and pl spectra. *RSC Advances*, 7(54):34244–34250, 2017.

[55] K. Kollbek, M. Sikora, Cz. Kapusta, J. Szlachetko, K. Zakrzewska, K. Kowalski, and M. Radecka. X-ray spectroscopic methods in the studies of nonstoichiometric tio2−x thin films. *Applied Surface Science*, 281:100–104, 2013.

[56] Robert Phillips and Charles W. Dunnill. Zero gap alkaline electrolysis cell design for renewable energy storage as hydrogen gas. *RSC Advances*, 6(102):100643–100651, 2016.

Eidesstattliche Erklärung

Hiermit versichere ich an Eides statt, dass ich diese Arbeit selbstständig verfasst und keine anderen als die angegebenen Quellen und Hilfsmittel benutzt habe. Außerdem versichere ich, dass ich die allgemeinen Prinzipien wissenschaftlicher Arbeit und Veröffentlichung, wie sie in den Leitlinien guter wissenschaftlicher Praxis der Carl von Ossietzky Universität Oldenburg festgelegt sind, befolgt habe.

Oldenburg, 22. Mai 2023